ARTICLE IN PRESS

LITHOS-01672; No of Pages 32

Available online at www.sciencedirect.com

ScienceDirect

LITHOS

Lithos xx (2007) xxx–xxx

www.elsevier.com/locate/lithos

# The dynamics of intra-oceanic subduction zones: A direct comparison between fossil petrological evidence (Rio San Juan Complex, Dominican Republic) and numerical simulation

M. Krebs [a,*], W.V. Maresch [a], H.-P. Schertl [a], C. Münker [b,e], A. Baumann [b], G. Draper [c], B. Idleman [d], E. Trapp [b]

[a] *Institut für Geologie, Mineralogie und Geophysik, Ruhr-Universität Bochum, D-44780 Bochum, Germany*

[b] *Institut für Mineralogie, Zentrallaboratorium für Geochronologie, Westfälische Wilhelms-Universität-Münster, Correnssstr. 24, D-48149 Münster, Germany*

[c] *Department of Earth Sciences, Florida International University, Miami, FL 33199, U.S.A.*

[d] *Department of Earth and Environmental Sciences, Lehigh University, 31 Williams Drive, Bethlehem, PA 18015, USA*

[e] *Mineralogisch-Petrologisches Institut, Universität Bonn, Poppelsdorfer Schloss, D-53115 Bonn, Germany*

Received 15 February 2006; accepted 3 September 2007



**Abstract**

Dispersed blocks of various types of metamorphic rocks in serpentinite mélanges of the northern Dominican Republic (Hispaniola) provide fossil evidence for the dynamics of the subduction zone channel in the intra-oceanic Caribbean subduction zone system between 120 and 55 Ma. Comprehensive petrological and geochronological data on three exemplary samples of eclogite and blueschist are presented that allow a series of different but interrelated pressure–temperature–time paths to be delineated. Eclogites indicate a low P/T gradient during subduction and record conditions in the nascent stages of the subduction zone. Lu–Hf data yield 103.6 ± 2.7 Ma for peak metamorphic conditions of 23 kbar/750 °C. An anticlockwise P–T path is defined. Other blocks record the continuous cooling of the evolving subduction zone and show typical clockwise P–T-paths. Omphacite blueschists reach maximum P–T-conditions of 17–18 kbar/520 °C at 80.3 ± 1.1 Ma (Rb–Sr age data). The mature subduction zone is typified by jadeite blueschists recording very high ("cold") P/T gradients. A Rb–Sr age of 62.1 ± 1.4 Ma dates peak metamorphic P–T conditions at 16–18 kbar/340–380 °C. The array of P–T–t data allows overall cooling rates of the subduction zone at depths of c. 60 km to be constrained at 9 °C/Ma. Cooling rates and exhumation rates (i.e., vertical component of retrograde trajectories) of the metamorphic blocks are 9–20 °C/Ma and 5–6 mm/a, respectively. The derived P–T–t array is compared with a 2-D numerical subduction-zone model published by Gerya et al. [Gerya, T.V., Stöckhert, B. and Perchuk, A.L., 2002. Exhumation of high-pressure metamorphic rocks in a subduction channel: a numerical simulation. Tectonics 142, 6-1-6-19.; 45° slab dip, 40 Ma lithosphere age, convergence rates of 10–40 mm/a], which incorporates weakening of lithospheric mantle of the hanging wall by fluids emanating from the downgoing slab, resulting in an increasingly more funnel-shaped subduction channel system with time. The numerically derived array of simulated P–T–t paths as well as the calculated rates of exhumation and cooling agree well with the P–T–t data derived from the metamorphic blocks of the Rio San Juan serpentinite mélanges when convergence rates of 15 to 25 mm/a are chosen. This value is also in accord with available paleogeographic reconstructions calling for a long-term average of

* Corresponding author.
*E-mail address:* martin.krebs@ruhr-uni-bochum.de (M. Krebs).

0024-4937/$ - see front matter © 2007 Published by Elsevier B.V.
doi:10.1016/j.lithos.2007.09.003

22 mm/a of orthogonal convergence. On the basis of the comparison, the onset of subduction in the Rio San Juan segment of the Caribbean Great Arc can be constrained to approximately 120 Ma. This segment was thus obviously active for more than 65 Ma. An orthogonal convergence rate of 15–25 mm/a requires that a minimum amount of 975–1625 km of oceanic crust must have been subducted. Both petrological/geochronological data and numerical simulation underscore the broad spectrum of different P–T–t paths and peak conditions recorded by material subducted at different periods of time as the subduction zone evolved and matured.


*Keywords:* Rio San Juan Complex; Eclogite; Omphacite blueschist; Jadeite blueschist; Anticlockwise P–T path; P–T pseudosection; Subduction rate; Exhumation rate; Great Caribbean Arc; Lu–Hf dating



## 1. Introduction

Pressure–temperature–time paths of rocks involved in high-pressure metamorphism in subduction zones can provide valuable information on the petrological and thermal structure as well as on the dynamics of plate convergence and mass movement in such collision zones. Ernst (1988) provided an early summary of known P–T-paths and showed how the different prograde and mainly retrograde trajectories can be logically used to identify specific geodynamic scenarios. Thus, P–T trajectories may show clockwise loops and essentially isothermal decompression. These can, for instance, be explained by rapid exhumation following cessation of subduction due to choking of the subduction zone by buoyant sialic crust (i.e., continental collision). "Hair-pin" type P–T paths with exhumation P–T trajectories essentially retracing burial trajectories indicate exhumation during active subduction. These require a concept of "two-way" flow in the subduction zone, such as provided by the corner flow model (Hsu, 1971; Cloos, 1982; Shreve and Cloos, 1986; Cloos and Shreve, 1988a,b), in which the motion of the down-going plate generates forced flow in a wedge-shaped subduction channel. Rheological considerations (e.g., Stöckhert, 2002; Gerya and Stöckhert, 2002; Gerya et al., 2002) support the necessary low bulk viscosity in such a channel. Increasing field-based evidence for the involvement of serpentinized peridotite from the overlying mantle wedge in the subduction channel (Blake et al., 1995; Guillot et al., 2000, 2001; Hermann et al., 2000; Schwartz et al., 2001) indicates that this channel could play a major role in subduction dynamics down to depths limited only by the stability of serpentine minerals (Wunder and Schreyer, 1997; Schmidt and Poli, 1998).

The corner flow model provides an explanation (e.g., Cloos, 1982; Gerya et al., 2002) for the existence of counterclockwise P–T paths (e.g., Wakabayashi, 1990; Krogh et al., 1994; Perchuk et al., 1999; Smith et al., 1999; Perchuk and Philippot, 2000), which should characterize early, nascent subduction zones, before the onset of significant downward migration of regional isotherms. Introducing the necessary time control on the P–T-paths of blueschist and eclogite-facies rocks is, thus, indispensable, but has proven to be more difficult. Comprehensive P–T–t-paths are essential if the thermal development of a subduction zone is to be monitored, or burial/exhumation and heating/cooling rates are to be understood. Most radiometric approaches provide cooling ages only, so that the high-temperature parts of the P–T–t paths often remain poorly defined, unless sophisticated techniques such as Lu–Hf or Nd–Sm systems (e.g., Thöni and Jagoutz, 1992; Duchene et al., 1997; Amato et al., 1999; Philippot et al., 2001) are used. An alternative is to model diffusion profiles in chemically discontinuous minerals such as garnets (e.g., Perchuk et al., 1999; Dachs and Proyer, 2002) along specific segments of the P–T–t path.

In the present study we present a comprehensive array of P–T–t paths characterizing an intra-oceanic subduction zone over a time span of more than 40 Ma. Isotopic age control is used, and the first Lu–Hf age dates in the Caribbean are reported. The samples were taken from the serpentinite mélanges of the Rio San Juan Complex of the northern Dominican Republic (Draper and Nagle, 1991), which can be interpreted to represent the preserved subduction channel of a major arc/subduction zone system (the "Great Arc" of Burke, 1988) that has swept through the Caribbean gap between North and South America since mid-Cretaceous time. The Lesser Antilles arc now represents the active segment of this system. We go on to view these petrological data within the context of a self-organizing numerical subduction zone model described by Gerya et al. (2002), adjusted for various convergence rates. This model allows for the progressive thermal, petrological and rheological modification of a starting subduction zone structure, and includes as a major feature a subduction-zone channel involving hydrated peridotites from the hanging-wall mantle wedge. The results corroborate the basic tenets and the approach of the numerical model on the one hand

Please cite this article as: Krebs, M., et al., The dynamics of intra-oceanic subduction zones: A direct comparison between fossil petrological evidence (Rio San Juan Complex, Dominican Republic) and numerical simulation, Lithos (2007), doi:10.1016/j.lithos.2007.09.003

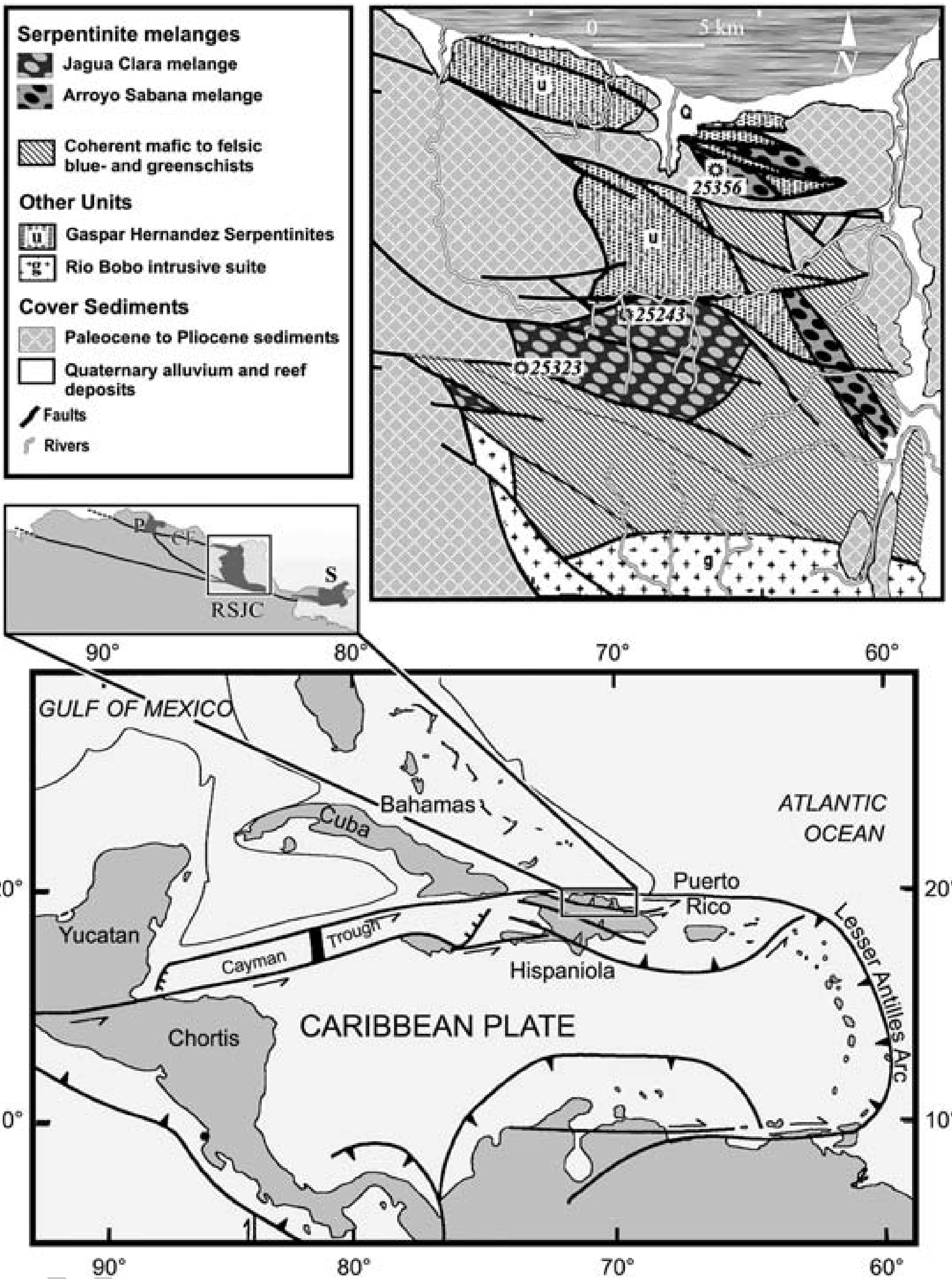


Fig. 1. Location map of the Rio San Juan Complex (RSJC) within the Caribbean and northern Dominican Republic (inset, P = Puerto Plata, S = Samaná Peninsula, CF = Camú Fault). Top right: Geological sketch map of the Rio San Juan Complex with sample locations of jadeite blueschist 25356, omphacite blueschist 25243 and eclogite 25323. Modified from Draper and Nagle (1991).

and also provide independent information on the subduction-zone parameters (i.e. slab dip, lithospheric age, convergence rate) of the Caribbean "Great Arc" on the other. They are also in accord with independently developed regional tectonic scenarios of the Caribbean area (e.g., Pindell et al., 2005).

## 2. The Rio San Juan complex

### 2.1. Geological setting

Serpentinite-matrix mélanges occur at several places in Cuba and Hispaniola (Lewis et al., 2006). Genetically, they are related to Cretaceous subduction processes at the leading edge of the eastward-drifting Caribbean plate and now decorating the trace of the Caribbean/North-American suture zone exposed in Cuba and Hispaniola.

Geologically, most of Hispaniola consists of an intra-oceanic island arc system that was active from Early Cretaceous to mid-Eocene time. During the late Paleogene and Neogene the arc edifice was deformed and the subsequent subsidence and uplift produced several sedimentary basins which now overlie the arc rocks. The exception to this general picture is the island's southern peninsula, which is an uplifted fragment of the 89 Ma Caribbean–Colombia Oceanic Plateau province that was attached to the rest of the island during the Neogene deformation.

The early history of the Hispaniola arc is controversial. Draper and others (1996) suggested that the pre-Aptian subduction zone dipped north. This early subduction ceased by Aptian time and was replaced by south dipping subduction on the northern side of the arc. Thus, the volcanic products of the Albian to mid-Eocene arc, were erupted through and onto the early arc.

The subduction zone rocks associated with the south-dipping, Late Cretaceous–Paleogene arc are found in the Cordillera Septentrional (Fig. 1). Blueschist/eclogite-facies metamorphic rocks and serpentinites are found in the Puerto Plata, Rio San Juan and Samaná regions. The Puerto Plata and Rio San Juan occurrences are essentially the same, as the Puerto Plata rocks were displaced approximately 50 km to the west of Rio San Juan by strike-slip displacement on the Camu fault (see insert, Fig. 1).

The Rio San Juan Complex (RSJC) is composed of three provinces (Draper and Nagle, 1991). The Cuaba Gneiss forms the southern part of the complex and consists of eclogitic gneisses retrograded to amphibolite facies. Recent work indicates that garnet peridotite and garnet pyroxenite pods in these gneisses experienced ultra-high-pressure conditions (Abbott et al., 2005a,b); as the gneisses most likely brought the pods to the

Table 1
List of mineral abbreviations used in this paper

| | |
|---|---|
| Agt | Aegirine–augite |
| Alm | Almandine |
| Ames | Amesite |
| Amp | Amphibole |
| Bar | Barroisite |
| Bt | Biotite |
| Cel | Celadonite |
| Chl | Chlorite |
| Clin | Clinochlore |
| Cpx | Clinopyroxene |
| Cz | Clinozoisite |
| Daph | Daphnite |
| Di | Diopside |
| Ep | Epidote |
| Fact | Ferroactinolite |
| Fcel | Fe-celadonite |
| Gl | Glaucophane |
| Gr | Grossular |
| Grt | Garnet |
| Hed | Hedenbergite |
| Jd | Jadeite |
| Lws | Lawsonite |
| Mg–Hbl | Magnesiohornblende |
| Mg–Kat | Magnesio katophorite |
| Mg–Tar | Magnesio taramite |
| Mt | Magnetite |
| Mu | Muscovite |
| Nam | Sodic amphibole |
| Omp | Omphacite |
| Pa | Paragonite |
| Parg | Pargasite |
| Phe | Phengite |
| Pl | Plagioclase |
| Py | Pyrope |
| Qtz | Quartz |
| Rt | Rutile |
| Tit | Titanite |
| W | Water |
| Win | Winchite |
| WR | Whole rock |
| Zir | Zircon |

Fig. 2. Photomicrographs of samples investigated (a: crossed polarizers, b-f: plane polarized light), g-h: backscatter images). a): Zoned sodic-calcic amphibole of the matrix with relics of pargasite (core) and glaucophane (outermost rim; eclogite 25323). b): Deformed garnet porphyroblast with omphacite, epidote, Mg-katophorite inclusions. Fractures within garnet contain secondary epidote, titanite and chlorite (eclogite 25323). c): Intertectonic omphacite, Mg-katophorite and pargasite rimmed by later glaucophane (eclogite 25323). d): Post-tectonic phengite, overgrowing newly formed glaucophane, barroisite, epidote, and omphacite. Rutile is accessory and rimmed by titanite (omphacite blueschist 25243). e): Metamorphic peak assemblage of jadeite, phengite, chlorite and glaucophane with accessory rutile rimmed by titanite (jadeite blueschist 25356). f): Intergrowth texture of jadeite+phengite+quartz replacing magmatic precursor minerals. Later glaucophane, phengite, chlorite, epidote, and rutile define a foliation $S_{n+1}$ (between jadeite grains the older foliation $S_n$ is still preserved; jadeite blueschist 25356). g): Inner part of zoned garnet porphyroblast with inclusions of the metamorphic peak assemblage epidote [B(1)], omphacite [B(1)], phengite[B(1)], and quartz. The post-tectonic rim of garnet contains inclusions of barroisite [C(1)], omphacite [C(1)], and phengite [C(1)] (eclogite 25323). h): Relic winchite and aegirine–augite of an older foliation $S_n$ preserved as inclusions in glaucophane and omphacite (omphacite blueschist 25243).



Please cite this article as: Krebs, M., et al., The dynamics of intra-oceanic subduction zones: A direct comparison between fossil petrological evidence (Rio San Juan Complex, Dominican Republic) and numerical simulation, Lithos (2007), doi:10.1016/j.lithos.2007.09.003

surface, then the gneisses themselves would also have experienced UHP conditions (Abbott and Draper, pers. communication, 2006). The central part of the RSJC is occupied by a large gabbro-diorite pluton, the Rio Boba Gabbro, which intrudes the Cuaba gneisses (Draper and Nagle, 1991). The northern part of the RSJC is the subject of this study and consists of coherent, fine-grained, blueschist–greenschist bodies faulted against serpentinite-matrix, blueschist–eclogite mélanges and other serpentinite bodies.

The age of unroofing of the RSJC is a little problematic. The Paleocene age Imbert Formation contains

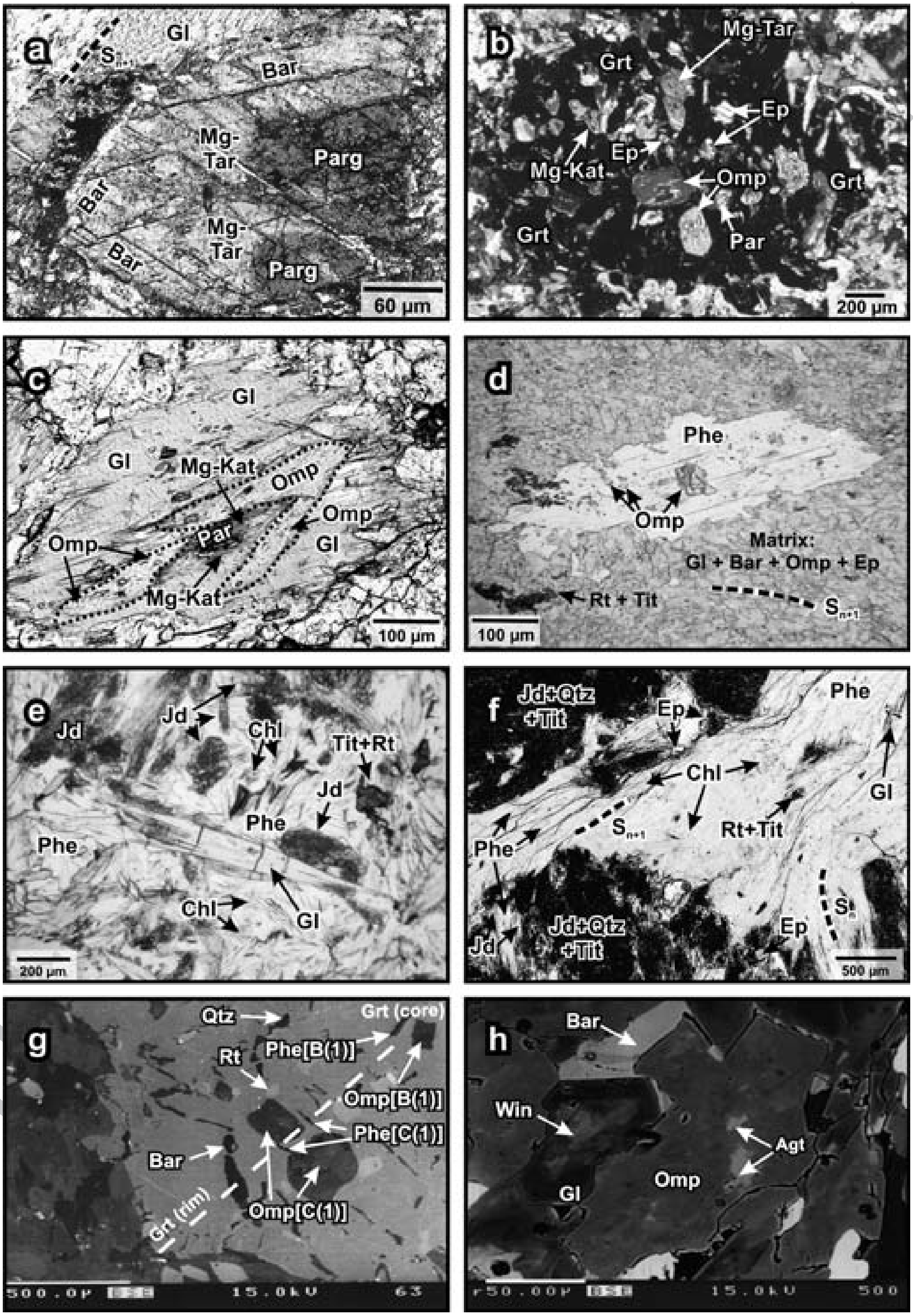


Please cite this article as: Krebs, M., et al., The dynamics of intra-oceanic subduction zones: A direct comparison between fossil petrological evidence (Rio San Juan Complex, Dominican Republic) and numerical simulation, Lithos (2007), doi:10.1016/j.lithos.2007.09.003

t2.1 Table 2

t2.2 Summary of key mineral assemblages, P–T-estimates and geochronological results defining the pressure–temperature–time paths of eclogite 25323, omphacite blueschist 25243 and jadeite blueschist 25356

| | Phase | Sample | P/T results | Geothermobarometer | Mineral assemblage | Age [Ma] | Method |
|---|---|---|---|---|---|---|---|
| t2.3 | | | | | | | |
| t2.4 | Pre A(1) | Eclogite 25323 | | | | 139.1±3.6 | U–Pb on Zir |
| t2.5 | A(1) | | 9.6–11.2 kbar | H | Omp-inclusions in garnet | | |
| t2.6 | | | 539–561 °C | K | | | |
| t2.7 | | | 596–617 °C | EG | | | |
| t2.8 | B(1) | | 23 kbar/ 750 °C | TWQ | Omp-, Ep-, and Phe-inclusions in garnet | 103.6±2.7 | Lu–Hf on Grt, Omp, Amp, Ep, WR |
| t2.9 | | | 23.9±1.6 kbar/ 694±46 °C | TH | | | |
| t2.10 | C(1) | | 22 kbar/ 565 °C | TWQ | Omp-, Amp-, and Phe-inclusions in garnet | 84 Interpolated (see text) | |
| t2.11 | | | 22.9±1.4 kbar/ 548±27 °C | TH | | | |
| t2.12 | D(1) | | 12 kbar/ 500 °C | TWQ | Gl, Chl, Phe, Qtz | 74.7±0.5 | Rb–Sr on Phe, Grt, WR |
| t2.13 | E(1) | | 6 kbar/ 350–400 °C | Interpolated from Fig. 6 | | 73.42±0.74 | Ar–Ar on Phe |
| t2.14 | A(2) | Omphacite blueschist 25243 | 11 kbar/ 400 °C | TWQ | Gl, Win, Agt, Ep Si-poor Phe, Qtz | – | |
| t2.15 | | | 9.9±1.7 kbar/ 378±52 °C | TH | | | |
| t2.16 | B(2) | | 17–18 kbar/ 520 °C | TWQ | Bar, Omp, Chl, Phe, Qtz | 80.3±1.1 | Rb–Sr on Phe, Amp, WR |
| t2.17 | | | 17.4±2.9 kbar/ 520±59 °C | TH | | | |
| t2.18 | C(2) | | 9–10 kbar/ 490 °C | TWQ | Mg–Hbl, $Fe^{3+}$-rich Ep, Chl, Pl, Qtz | – | |
| t2.19 | | | 7.7±2.1 kbar/ 517±68 °C | TH | | | |
| t2.20 | D(2) | | 6 kbar/ 350–400 °C | Interpolated from Fig. 7 | | 73.85±0.79 | Ar–Ar on Phe |
| t2.21 | B(3) | Jadeite blueschist 25356 | 16–18 kbar/ 340–380 °C | TWQ | Jd, Gl, Phe, Chl, Qtz | 62.1±1.4 | Rb–Sr on Phe, Amp, WR |

t2.22 EG = Ellis and Green (1979); K = Krogh (1988); H = Jadeite-content in Cpx (Holland, 1979, 1980, 1983); TWQ = TWQ Berman (Jan92.gsc), Evans (1990) and Vidal et al. (2001); TH = Thermocalc 3.1(Holland and Powell, 1998a,b; data-set June 2001).

t2.23 (A) = burial-related phases; (B) = peak-metamorphic phases; (C), (D) = exhumation-related phases.

conglomerate layers with poorly rounded clasts of serpentinite and metamorphic rocks. These could be derived from the erosion of the RSJC, but as subduction was still occurring at this time, there is also the possibility that they could be deposits derived from a fore-arc serpentinite mud volcano, such as those found in the modern day Marianas arc (Fryer et al., 1999). Tertiary clastic sediments nonconformably overlie the crystalline rocks, although Neogene transpressive deformation has produced several strike-slip and thrust fault contacts. The age of the sediments overlying the complex is uncertain, but elsewhere in the Cordillera Septentrional, they range in age from Late Eocene to Early Miocene.

The RSJC mélanges form a hummocky terrain. The blocks are relatively small and range from about 1 m to 10 m in diameter. Blocks that are observed in contact with the matrix have 20–30 cm thick, metasomatic rinds consisting of coarse-grained actinolite, chlorite and fuchsite. Many blocks lie on the ground with no attached matrix and incomplete metasomatic rinds suggesting that many blocks form a lag deposit that has concentrated the blocks from the three dimensional mélange at the surface. Thus, our surface collection likely samples a large volume of the original mélange.

The blocks show a range of deformation. Some blocks exhibit practically no foliation, whereas others have moderate to highly developed foliations. Most blocks with highly developed foliations also have strongly developed mineral lineations, and among these some show the development of doubly-vergent folds whose axes are parallel to the lineation (i.e. these are sheath folds).



Please cite this article as: Krebs, M., et al., The dynamics of intra-oceanic subduction zones: A direct comparison between fossil petrological evidence (Rio San Juan Complex, Dominican Republic) and numerical simulation, Lithos (2007), doi:10.1016/j.lithos.2007.09.003

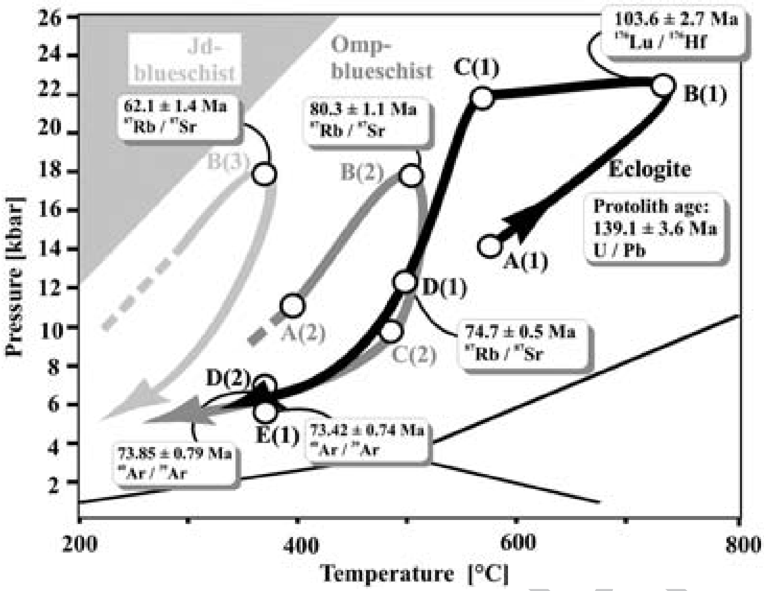


Fig. 3. Summary of the P–T-paths derived for eclogite 25323, omphacite blueschist 25243 and jadeite blueschist 25356. The geochronological results are taken from Figs. 10–12.

## 2.2. Sampling

The blocks of metamorphic rocks encountered in the Rio San Juan serpentinite mélanges represent a variety of lithologies comprising various types of basic to intermediate magmatic protoliths such as blueschists (with garnet, lawsonite, omphacite, jadeite), eclogite and amphibolite. Massive lawsonite–glaucophane rocks occur. Granitic and trondhjemitic orthogneisses are common. Metapelites are subordinate. This paper draws on a detailed study of some 200 samples (Krebs, 2006) collected in two field campaigns in 2000 and 2001. Previous mapping, sampling and laboratory studies (Draper and Nagle, 1991; Anam, 1994) served as invaluable sources of information for obtaining a representative cross-section of the various lithologies entrained in the Rio San Juan mélanges.

Detailed microanalytical data, which allow pressure–temperature paths to be derived are available for some 30 samples. Geochronological data have been obtained on 10 of these samples. As a result, it has become possible to elucidate the details of mass movement in the Rio San Juan mélanges. A comprehensive description of these results will be presented elsewhere (Krebs, 2006). In the present paper, we describe three typical pressure–temperature–time paths that characterize the development of the Rio San Juan subduction zone over a time span of approximately 50–60 Ma. These data have been obtained for an eclogite (sample no. 25323), as well as for an omphacite-bearing (sample no. 25243) and a jadeite-bearing (sample no. 25356) blueschist. We go on to compare these P–T–t paths with those obtained from a self-organizing numerical simulation calculated with boundary conditions representing the Rio San Juan subduction zone as closely as possible.

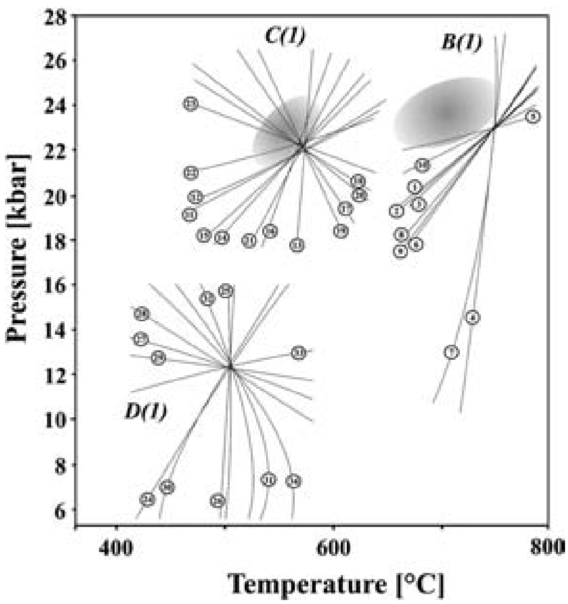


Fig. 4. Estimates for P–T coordinates B(1), C(1) and D(1) of eclogite 25323 P–T-path using the TWQ-method (for numbered reactions see Table 3) and THERMOCALC average P–T method (Powell and Holland, 1994; grey ellipses) for the mineral assemblages summarized in Table 2.



Please cite this article as: Krebs, M., et al., The dynamics of intra-oceanic subduction zones: A direct comparison between fossil petrological evidence (Rio San Juan Complex, Dominican Republic) and numerical simulation, Lithos (2007), doi:10.1016/j.lithos.2007.09.003

Table 3
Phase equilibria generated from the TWQ calculation of eclogite 25323 (Fig. 3)

| No. | Stage B(1) |
|---|---|
| 1 | 3 cel + alm + 2 gr = 3 mu + 3 hed + 3 di |
| 2 | 3 di + alm = 3 hed + py |
| 3 | 2 cz + jd + cel = pa + di + gr + mu + qtz |
| 4 | 4 cz + 2 jd + alm + 5 cel = 2 pa + 5 di + 3 hed + 5 mu + 2 qtz |
| 5 | 3 di + 3 jd + 6 cz = 3 qtz + py + 5 gr + 3 pa |
| 6 | 3 cel + 2 alm + 2 gr = py + 3 mu + 6 hed |
| 7 | py + 2 gr + 3 cel = 6 di + 3 mu |
| 8 | 12 cz + 6 jd + 3 cel = 6 pa + 8 gr + 3 mu + py + 6 qtz |
| 9 | 12 cz + 6 jd + 8 alm + 15 cel = 6 pa + 24 hed + 15 mu + 5 py + 6 qtz |
| 10 | 4 cz + py + 2 jd + 5 cel = 2 pa + 8 di + 5 mu + 2 qtz |
| | |
| | Stage C(1) |
| 11 | 5 alm + 24 di + gr + 6 jd + 6 $H_2O$ = 12 qtz + 15 hed + 6 parg |
| 12 | 3 alm + 17 di + 4 jd + mu + 4 $H_2O$ = 8 qtz + 9 hed + cel + 4 parg |
| 13 | 3 di + alm = 3 hed + py |
| 14 | 3 cel + alm + 2 gr = 3 mu + 3 hed + 3 di |
| 15 | 6 jd + 17 gr + 13 alm + 24 cel + 6 $H_2O$ = 6 parg + 39 hed + 24 mu + 12 qtz |
| 16 | 2 parg + 5 cel + 3 gr + 4 qtz = 5 mu + 2 jd + 13 di + 2 $H_2O$ |
| 17 | 8 py + 6 jd + 9 hed + gr + 6 $H_2O$ = 6 parg + 3 alm + 12 qtz |
| 18 | 5 py + 6 jd + gr + 9 di + 6 $H_2O$ = 6 parg + 12 qtz |
| 19 | 17 py + 3 mu + 12 jd + 24 hed + 12 $H_2O$ = 12 parg + 3 cel + 8 alm + 24 qtz |
| 20 | 3 py + mu + 4 jd + 8 di + 4 $H_2O$ = 4 parg + cel + 8 qtz |
| 21 | 3 cel + 2 alm + 2 gr = py + 3 mu + 6 hed |
| 22 | 3 cel + 2 gr + py = 3 mu + 6 di |
| 23 | 13 py + 12 jd + 8 gr + 9 cel + 12 $H_2O$ = 12 parg + 9 mu + 24 qtz |
| | |
| | Stage D(1) |
| 24 | daph + 5 cel = 5 fcel + clin |
| 25 | 4 qtz + 6 gl + 13 ames + 70 fcel + 10 $H_2O$ = 70 cel + 12 pa + 14 daph |
| 26 | 4 cel + daph + mu = ames + 5 fcel |
| 27 | 4 qtz + 6 gl + 13 ames + 10 $H_2O$ = 12 pa + 14 clin |
| 28 | 5 fcel + 5 ames = 5 mu + 4 clin + daph |
| 29 | ames + cel = clin + mu |
| 30 | 8 qtz + 35 mu + 12 gl + 7 daph + 20 $H_2O$ = 35 fcel + 24 pa + 9 ames |
| 31 | 4 qtz + 14 mu + 6 gl + 10 $H_2O$ = 14 cel + 12 pa + ames |
| 32 | 4 qtz + 13 mu + 6 gl + 5 fcel + 10 $H_2O$ = 18 cel + 12 pa + daph |
| 33 | 20 qtz + 65 mu + 30 gl + 13 daph + 50 $H_2O$ = 65 fcel + 60 pa + 18 clin |
| 34 | 4 qtz + 13 mu + 6 gl + 10 $H_2O$ = 13 cel + 12 pa + clin |

Pertinent electron microprobe analyses are given in the Appendix.

### 2.3. Petrography

The mineral abbreviations used in this paper are defined in Table 1.

*Eclogite* (sample 25323) contains garnet and omphacite as main constituents with minor amounts of epidote, chlorite, phengite, sodic–calcic (taramite, katophorite, barroisite) and calcic amphibole (pargasite, actinolite). Glaucophane, quartz, titanite, rutile, magnetite and plagioclase are accessories. The main-foliation is defined by columnar to platy omphacite, epidote, sodic-calcic amphiboles, phengite, chlorite and rutile. The sodic–calcic amphiboles of the matrix (taramite, katophorite, barroisite) have an oblique orientation to $S_{n+1}$ (partly recrystallized relics of an older foliation $S_n$) and contain relics of calcic amphibole (pargasite) (Fig. 2a). The $S_{n+1}$-foliation wraps around zoned garnet porphyroblasts that partly develop post-tectonic or late inter-tectonic rims. These complex zoned garnets contain systematically arranged types of inclusions (Fig. 2b and g) with calcic amphibole (pargasite), omphacite (low in jadeite component), epidote (high in $Fe^{3+}$), and titanite in the core and sodic-calcic amphibole (katophorite, barroisite), jadeite-rich omphacite, phengite, epidote (low in $Fe^{3+}$), and rutile in the rim. Randomly oriented actinolite, epidote, phengite, and chlorite are post-tectonic, as are the rims of glaucophane around barroisite, Mg-katophorite and omphacite (Fig. 2c).

*Omphacite blueschist* (sample 25243) contains omphacite, epidote, zoisite, sodic–(glaucophane) and sodic–calcic amphibole (barroisite) as main constituents; chlorite, white mica and calcic amphibole (actinolite, magnesio-hornblende) occur in minor, and quartz, titanite, and rutile in accessory amounts. The main $S_{n+1}$ foliation in this sample is primarily defined by newly formed and/or re-crystallized undeformed glaucophane/barroisite, epidote, and phengite. Deformed glaucophane, winchite, phengite, epidote, zoisite, titanite, and aegirine–augite (generally as inclusions in omphacite see Fig. 2h) are oriented oblique to $S_{n+1}$ and define an older foliation $S_n$ in rare microlithon relics. Late deformational events are recorded as fractures parallel to $S_{n+1}$, which are filled by randomly oriented

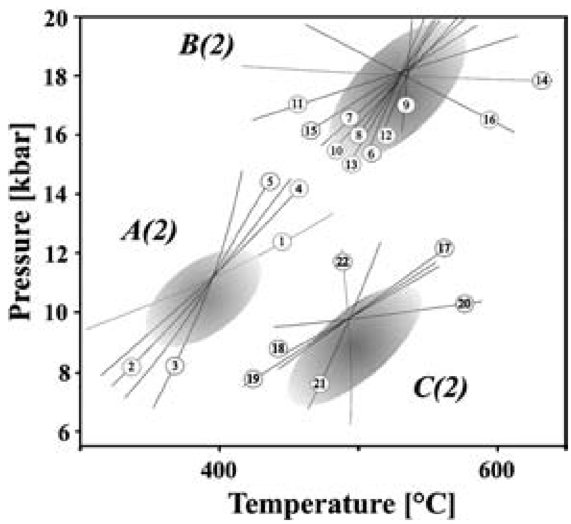


Fig. 5. Estimates for P–T coordinates A(2), B(2) and C(2) of omphacite blueschist (sample 25243) P–T-path using the TWQ-method (for numbered reactions see Table 4) and THERMOCALC average P–T method (Powell and Holland, 1994; grey ellipses) for the mineral assemblages summarized in Table 2.



Please cite this article as: Krebs, M., et al., The dynamics of intra-oceanic subduction zones: A direct comparison between fossil petrological evidence (Rio San Juan Complex, Dominican Republic) and numerical simulation, Lithos (2007), doi:10.1016/j.lithos.2007.09.003

Table 4
Phase equilibria generated from the TWQ calculation for omphacite blueschist 25243 (Fig. 4)

| No. | Stage A(2) |
|---|---|
| 1 | fact+5 cel+2 jd=gl+2 di+5 fcel |
| 2 | cel+gl+2 cz=qtz+mu+4 di+2 pa |
| 3 | 10 fcel+3 gl+2 cz=qtz+mu+4 jd+2 pa+9 cel+2 fact |
| 4 | fact+6 cel+2 jd+2 cz=qtz+mu+6 di+2 pa+5 fcel |
| 5 | 5 fcel+6 gl+10 cz=5 qtz+5 mu+2 jd+18 di+10 pa+fact |
| | |
| | Stage B(2) |
| 6 | 2 cz+11 qtz+7 mu+13 jd+3 daph+8 cel=2 parg+15 fcel+11 pa |
| 7 | 2 cz+11 qtz+4 mu+13 jd+3 ames=2 parg+4 cel+11 pa |
| 8 | 2 cz+11 qtz+7 mu+13 jd+3 clin=2 parg+7 cel+11 pa |
| 9 | mu+daph+4 cel=5 fcel+ames |
| 10 | 2 cz+11 qtz+5 mu+13 jd+2 ames+daph=2 parg+5 fcel+11 pa |
| 11 | 2 cz+11 qtz+13 jd+7 ames+20 fcel=2 parg+20 cel+11 pa+4 daph |
| 12 | Daph+5 cel=5 fcel+clin |
| 13 | cz+55 qtz+35 mu+65 jd+8 clin+7 daph=10 parg+35 fcel+55 pa |
| 14 | cel+ames=mu+clin |
| 15 | 2 cz+11 qtz+13 jd+7 ames=2 parg+11 pa+4 clin |
| 16 | 5 fcel+5 ames=5 mu+4 clin+daph |
| | |
| | Stage C(2) |
| 17 | 20 gl+12 cz=34 qtz+28 ab+3 ames+12 parg+2 $H_2O$ |
| 18 | 6 cz+13 gl+2 $H_2O$=6 parg+20 ab+3 clin+17 qtz |
| 19 | 6 cz+11 gl=6 parg+ames+16 ab+clin+17 qtz |
| 20 | 2 gl+ames+2 $H_2O$=4 ab+2 clin |
| 21 | 7 clin+3 gl+6 cz=17 qtz+5 ames+6 parg+8 $H_2O$ |
| 22 | 34 qtz+13 ames+12 parg+22 $H_2O$=12 ab+20 clin+12 cz |

Pertinent electron microprobe analyses are given in the Appendix.

barroisite, epidote, titanite and quartz. In addition, late post-tectonic epidote, phengite, albite, and calcic amphibole overgrow the main $S_{n+1}$-foliation (Fig. 2d).

The main constituents of *jadeite blueschist* (sample 25356) are jadeite, glaucophane, phengite, and quartz. Epidote and chlorite occur as minor amounts, while titanite, rutile, magnetite, and albite are accessories (Fig. 2e). Glaucophane, phengite, chlorite, epidote, and titanite inclusions define relics of an old $S_n$ foliation, which is preserved in microlithons between the cleavage domains of a younger $S_{n+1}$ foliation. The $S_{n+1}$-foliation is present as parallel to sub-parallel, newly crystallized glaucophane, phengite, chlorite, epidote, and rutile. Jadeite porphyroblasts, together with phengite, appear to replace magmatic precursors (such as K-feldspar). The $S_n$ and $S_{n+1}$ foliations are deflected by the older jadeite porphyroblasts (Fig. 2f). In addition, late undeformed jadeite grains overgrow the youngest foliation $S_{n+1}$. Randomly oriented aggregates of chlorite and epidote as well as titanite rims around rutile also grew post-tectonically and were formed after $S_{n+1}$.

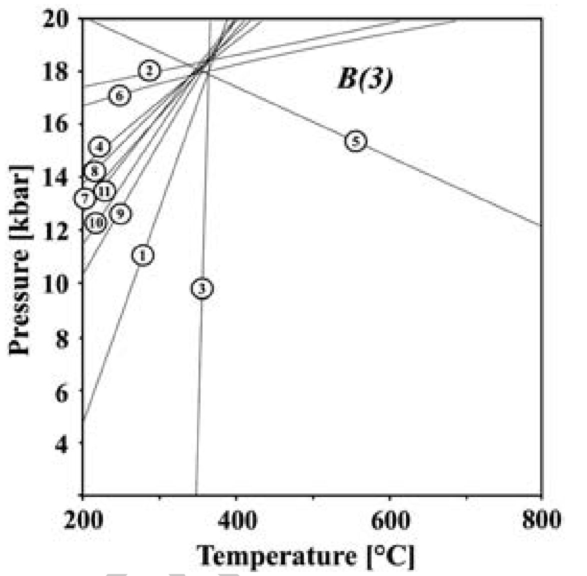


Fig. 6. Estimate for P–T coordinate B(3) of jadeite blueschist (sample 25356) P–T-path using the TWQ-method (for numbered reactions see Table 5) for the mineral assemblage summarized in Table 2.

### 2.4. P–T paths

To provide detailed insight into the pressure–temperature history of the above representative samples, constituent minerals were analyzed by electron microprobe and the mineral assemblages evaluated using classical thermobarometers, multi-equilibrium calculations and P–T pseudosections. Analysis of compositional zoning and inclusion relationships played a key part in deriving comprehensive P–T paths. The classical thermobarometers used included garnet–clinopyroxene (Ellis and Green, 1979; Krogh, 1988), garnet–clinopyroxene-phengite (Waters and Martin, 1993; Carswell et al., 1997), jadeite-content in clinopyroxene (Holland, 1979, 1980,

Table 5
Phase equilibria generated from the TWQ calculation of jadeite blueschist 25356 (Fig. 5)

| No. | Stage B(3) |
|---|---|
| 1 | Daph+5 Cel=5 Fcel+Clin |
| 2 | 6 Qtz+5 Jd+2 Ames+5 Fcel=5 Cel+3 Pa+Daph+Gl |
| 3 | 4 Cel+Daph+Mu=Ames+5 Fcel |
| 4 | 2 Ames+5 Jd+6 Qtz=Gl+Clin+3 Pa |
| 5 | 5 Fcel+5 Ames=5 Mu+4 Clin+Daph |
| 6 | Cel+Ames=Mu+Clin |
| 7 | 24 Qtz+5 Mu+20 Jd+3 Ames+Daph=5 Fcel+12 Pa+4 Gl |
| 8 | 6 Qtz+Mu+5 Jd+Ames=Cel+3 Pa+Gl |
| 9 | 3 Cel+Daph+5 Jd+2 Mu+6 Qtz=Gl+3 Pa+5 Fcel |
| 10 | 30 Qtz+10 Mu+25 Jd+3 Clin+2 Daph=10 Fcel+15 Pa+5 Gl |
| 11 | 6 Qtz+2 Mu+5 Jd+Clin=2 Cel+3 Pa+Gl |

Pertinent electron microprobe analyses are given in the Appendix.



Please cite this article as: Krebs, M., et al., The dynamics of intra-oceanic subduction zones: A direct comparison between fossil petrological evidence (Rio San Juan Complex, Dominican Republic) and numerical simulation, Lithos (2007), doi:10.1016/j.lithos.2007.09.003

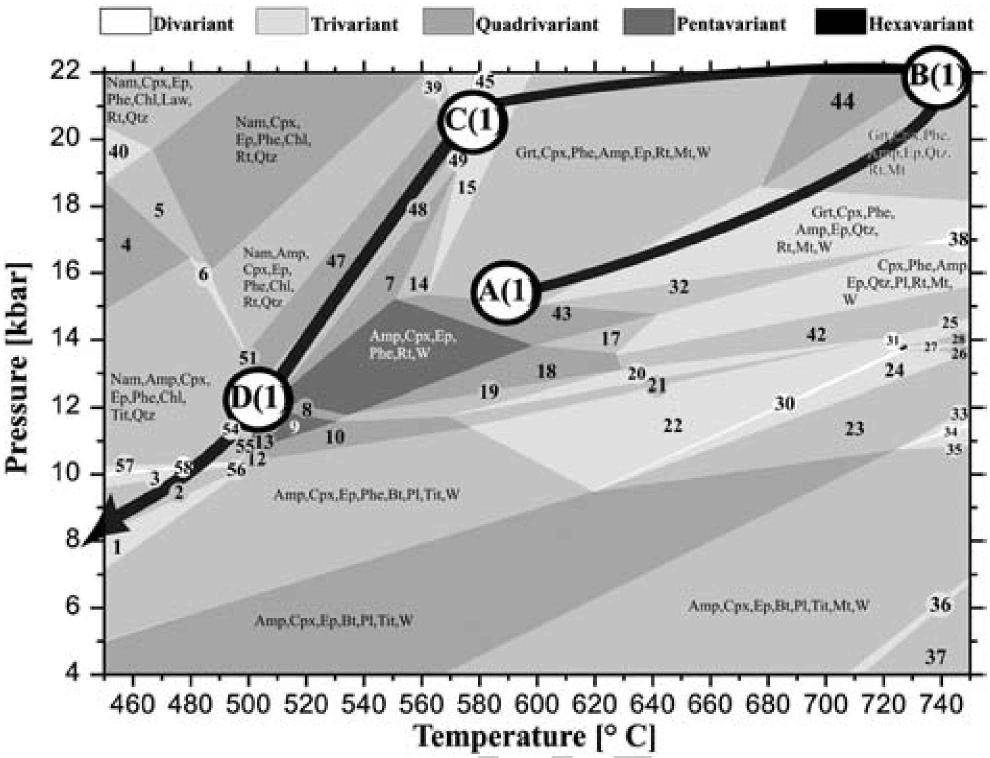


Fig. 7. P–T pseudosection constructed for eclogite 25323 in the system KNCFFMASTH (P–T-path coordinates A(1) to D(1) from Fig. 3). Details of numbered phase fields are given in Table 6.



1983), and the tetrahedral Si content in phengite (Massonne and Szpurka, 1997). Multi-equilibrium calculations were performed employing the programs *Thermocalc 3.1* (Holland and Powell, 1998a; upgraded dataset of Holland and Powell, June 2001) and TWQ, based on the dataset of Berman (1988; Jan92.gsc supplemented by data from Evans, 1990; Vidal et al., 2001). The P–T pseudosections were obtained with the programs *Thermocalc 3.1* (Holland and Powell, 2001) and *Dekap* (Gerya et al., 2001; Holland and Powell, 2001) in the system $K_2O$–$Na_2O$–CaO–$Fe_2O_3$–FeO–MgO–$Al_2O_3$–$SiO_2$–$TiO_2$–$H_2O$ (KNCFFMASTH) from whole-rock compositions of the samples. The mineral analyses providing the analytical data base in this study and the activity models used for the thermodynamic calculations are summarized in the Appendix (Table A1 and Table A2).

The pressure–temperature paths of the three exemplary samples are summarized in Table 2 and depicted in Fig. 3. For descriptive purposes, we use the following code in this paper. Stage "A" denotes the prograde burial-related phase and "B" the peak-metamorphic conditions, whereas "C" and "D" pertain to the exhumation-related phase. The numbers in brackets refer to the paths derived from eclogite (1), omphacite blueschist (2), and jadeite blueschist (3). We begin by describing the P–T-results obtained from "classical" thermobarometric and multi-equilibria calculations (Figs. 4–6), which are subsequently viewed within the context of P–T pseudosections for each rock (Figs. 7–9).

In *eclogite* 25323, systematically arranged inclusions of omphacite, amphibole, epidote and phengite in the cores (only omphacite epidote and amphibole) and rims (omphacite, epidote, amphibole and phengite) of zoned garnet porphyroblasts (pre-$S_{n+1}$ to post $S_{n+1}$) record a prograde path with a flat ("hot") P/T-gradient. Maximum P–T conditions are 750 °C and 23 kbar (stages A(1) to B (1) in Fig. 4), followed by subsequent isobaric cooling to 565 °C and 22 kbar (stages B(1) to C(1)). The late growth of glaucophane, chlorite, phengite, and quartz yields P–T conditions of 500 °C/12 kbar (stage D(1) in Fig. 4), which are related to the return path.

The prograde development of *omphacite blueschist* 25243 can be traced with multi-equilibria calculations (TWQ) of the phases defining the old foliation $S_n$ (i.e. deformed glaucophane, winchite, aegirine–augite, epidote, Si-poor phengite, and quartz, i.e. representing stage A(2) in Fig. 5 and Table 2. This prograde P/T path is clearly steeper than in the eclogite above. Multi-equilibria calculations based on the minerals aligned in $S_{n+1}$ (barroisite, Al-rich epidote, glaucophane, phengite,

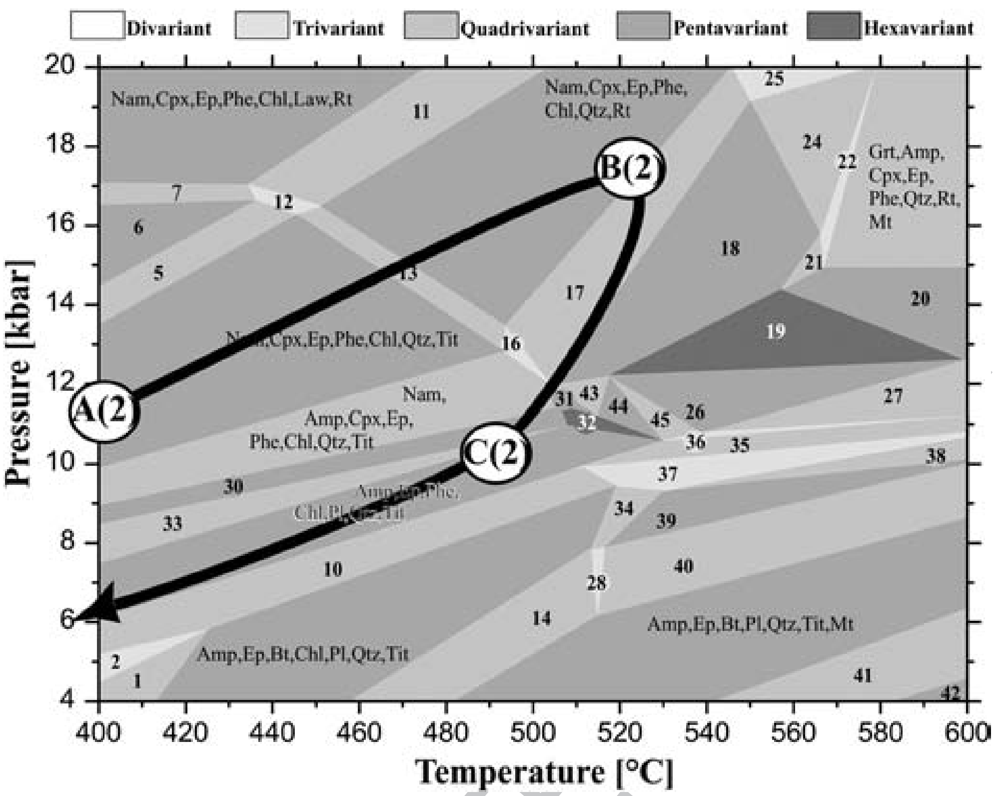


Fig. 8. P–T pseudosection constructed for omphacite blueschist 25243 in the system KNCFFMASTH (P–T-path coordinates A(2) to C(2) from Fig. 4). Details of numbered phase fields are given in Table 6.

chlorite, omphacite) yield peak metamorphic conditions of about 520 °C/17–18 kbar (stage B(2) in Fig. 5). During the retrograde stage, P–T conditions of 490 °C/9–10 kbar are derived from reactions involving the post-tectonic phases magnesiohornblende, chlorite, $Fe^{3+}$-rich epidote, plagioclase, and quartz (stage C(2) in Fig. 5).

*Jadeite blueschist* 25356 clearly experienced the steepest ("coldest") prograde P/T-gradient. Calculation of multi-variant phase equilibria (TWQ) including jadeite, phengite, chlorite, glaucophane and quartz yields P–T conditions of 340–380 °C and 16–18 kbar (stage B(3) in Fig. 6).

The anticlockwise P–T path derived for *eclogite* 25323 fits nicely into the picture obtained from the P–T pseudosection (Fig. 7): The presence of quartz inclusions in garnet constrains the prograde P–T path to cross the quartz-bearing trivariant field Grt+Cpx (with omphacitic composition)+Phe+Amp (pargasite)+Ep+Qtz+Rt+Mt+W and the quadrivariant field Grt+Cpx (omphacite)+Phe+Amp (taramite)+Ep+Qtz+Rt+Mt. Fig. 6 also documents the reason for the observed compositional changes in the amphiboles (pargasite→taramite→katophorite→barroisite) during subduction and isobaric cooling (stages A(1) to C(1)). In moving along the indicated path (A(1) to C(1)), pargasite (the stable amphibole in the trivariant field Grt+Cpx+Phe+Amp+Ep+Qtz+Rt+Mt+W) changes its composition to taramite after entry in the quadrivariant field Grt+Cpx (omphacitic composition)+Phe+Amp+Ep+Qtz+Rt+Mt. Crossing the quadrivariant field Grt+Cpx (omphacite)+Phe+Amp+Ep+Rt+Mt+W stabilizes an amphibole of katophoritic composition instead of taramite. With decreasing temperature, katophorite is replaced by barroisite as the P–T path enters the trivariant field 15 (Grt+Cpx (omphacite)+Phe+Chl+Amp+Ep+Rt+Mt+W). This trivariant field also illustrates the late growth of chlorite. Finally the formation of titanite rims around rutile and glaucophane rims around barroisite provides some constraints on the retrograde P–T path. Titanite grows after entry into the quadrivariant field 51 (Amp+Cpx+Ep+Phe+Chl+Tit+Rt+Qtz) and glaucophane appears when the trivariant field 54 (Nam+Amp+Cpx+Ep+Phe+Chl+Tit+Qtz+W) is reached (stages D(1) and post D(1)). The absence of biotite restricts further uplift to PT-conditions defined by the quadrivariant field 2 (Amp+Cpx+Ep+Phe+Chl+Pl+Tit+W).

In general, the P–T pseudosection derived for *omphacite blueschist* 25243 (Fig. 8) corroborates the calculated

Please cite this article as: Krebs, M., et al., The dynamics of intra-oceanic subduction zones: A direct comparison between fossil petrological evidence (Rio San Juan Complex, Dominican Republic) and numerical simulation, Lithos (2007), doi:10.1016/j.lithos.2007.09.003

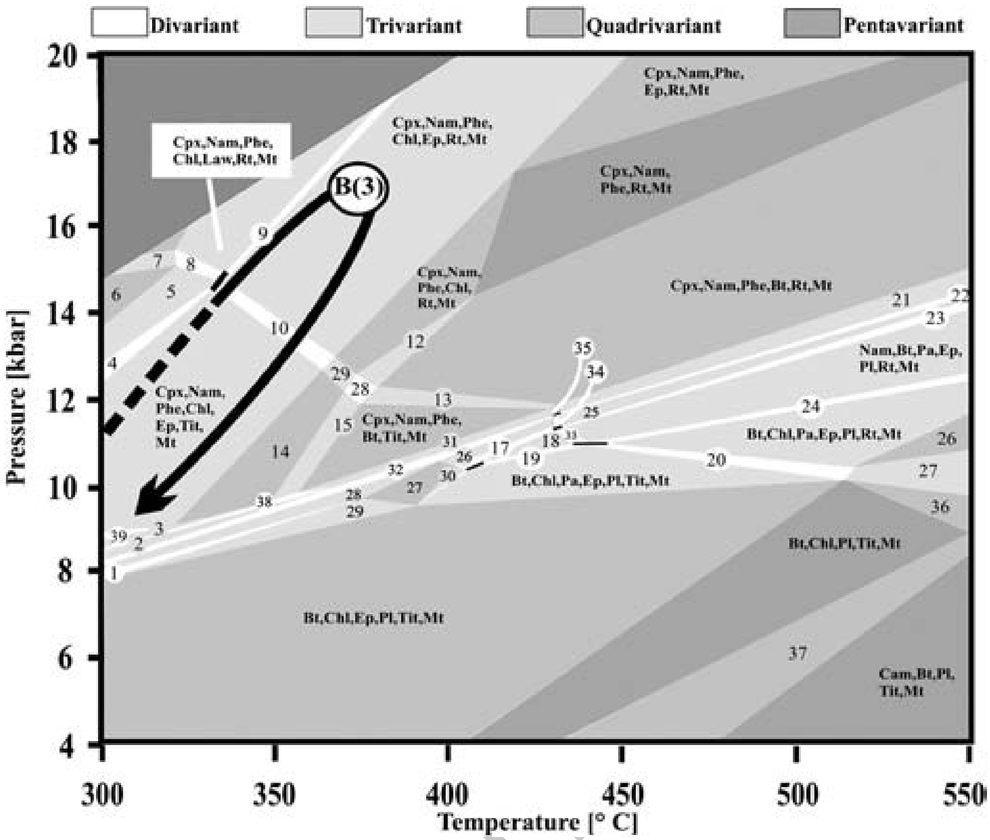


Fig. 9. P–T pseudosection constructed for jadeite blueschist 25356 in the system KNCFFMASTH (P–T-path coordinate B(3) from Fig. 5). Details of numbered phase fields are given in Table 6. Include quartz and water in all fields shown.

P–T conditions. A(2) lies within the pentavariant field of Nam (glaucophane)+Cpx (with the composition of Na-rich-augite)+Ep+Phe+Chl+Tit+Qtz, thus comprising all the phases oriented parallel to $S_n$. During the burial-related stages A(2)–B(2) (see Fig. 9), clinopyroxene (Na-rich-augite) changes its composition towards omphacite, titanite reacts out, and barroisite as well as rutile reacts in. Along the return path B(2)–C(2) barroisite is replaced by magnesiohornblende and rutile by titanite (when the quadrivariant field Nam+Amp+Cpx+Ep+Phe+Chl+Tit+Qtz is reached). Thereafter (post-C(2)), plagioclase reacts in (quadrivariant field 33: Nam+Amp+Ep+Phe+Chl+Pl+Tit+Qtz) and glaucophane disappears (pentavariant field Amp+Ep+Phe+Chl+Pl+Qtz). The absence of biotite and the replacement of glaucophane constrains further uplift to a small corridor defined by the pentavariant field Amp+Ep+Phe+Chl+Pl+Qtz+Tit.

The P–T pseudosection of *jadeite blueschist* 25356 (Fig. 9) provides important additional information, especially for the return path. The prograde path derived from thermobarometry encounters a trivariant field with the assemblage Cpx (jadeite)+Nam (glaucophane)+Phe+Chl+Ep+Tit+Mt+Qtz (+W), which is also the assemblage observed in thin-section constituting the old foliation $S_n$. With increasing pressure and temperature rutile replaces titanite, again consistent with the observations in thin-section. The resulting trivariant assemblage Cpx (jadeite)+Nam (glaucophane)+Phe+Chl+Ep+Rt+Mt+Qtz (+W) represents peak metamorphic conditions (B(3) in Fig. 9). Observations in thin-section demonstrate that chlorite and epidote are stable during retrograde metamorphism. Therefore the retrograde P–T path must be characterized by strong cooling during return, and thus the retrograde P–T-gradient of the path must be very similar to the prograde one (see Fig. 9). If the retrograde path were close to isothermal, chlorite+epidote would be expected to react out, and biotite should react in. Neither reaction is observed in thin-section. The P–T pseudosection also explains the absence of lawsonite and any calcic amphibole, since lawsonite would only be stable at higher pressures and lower temperatures, whereas the formation of calcic amphiboles would require higher temperatures.

The above three types of P–T paths can be considered to be typical for blocks in the Rio San Juan

Please cite this article as: Krebs, M., et al., The dynamics of intra-oceanic subduction zones: A direct comparison between fossil petrological evidence (Rio San Juan Complex, Dominican Republic) and numerical simulation, Lithos (2007), doi:10.1016/j.lithos.2007.09.003

Table 6
Definition of numbered phase fields in the pseudosections of Figs. 6–8

Jadeite blueschist 25356

| No. | Assemblage (+Qtz+W) |
|---|---|
| 1 | Cpx,Phe,Bt,Chl,Ep,Pl,Tit,Mt |
| 2 | Cpx,Nam,Phe,Bt,Pl,Tit,Mt |
| 3 | Cpx,Phe,Nam,Chl,Pl,Tit,Mt |
| 4 | Cpx,Nam,Phe,Chl,Law,Ep,Tit,Mt |
| 5 | Cpx,Nam,Phe,Chl,Law,Tit,Mt |
| 6 | Cpx,Nam,Phe,Chl,Law,Tit,Mt,-W |
| 7 | Cpx,Nam,Phe,Chl,Law,Rt,Tit,Mt,-W |
| 8 | Cpx,Nam,Phe,Chl,Law,Rt,Tit,Mt |
| 9 | Cpx,Nam,Phe,Chl,Law,Ep,Rt,Mt |
| 10 | Cpx,Nam,Phe,Chl,Ep,Rt,Tit,Mt |
| 11 | Cpx,Nam,Phe,Chl,Rt,Mt |
| 12 | Cpx,Nam,Phe,Bt,Chl,Rt,Mt |
| 13 | Cpx,Nam,Phe,Bt,Rt,Tit,Mt |
| 14 | Cpx,Nam,Phe,Chl,Tit,Mt |
| 15 | Cpx,Nam,Phe,Bt,Chl,Tit,Mt |
| 16 | Cpx,Bt,Chl,Pa,Ep,Pl,Tit,Mt |
| 17 | Cpx,Nam,Bt,Pa,Ep,Pl,Tit,Mt |
| 18 | Nam,Bt,Pa,Ep,Pl,Tit,Mt |
| 19 | Nam,Bt,Chl,Pa,Ep,Pl,Tit,Mt |
| 20 | Bt,Chl,Pa,Ep,Pl,Rt,Tit,Mt |
| 21 | Cpx,Nam,Phe,Bt,Pl,Rt,Mt |
| 22 | Cpx,Nam,Phe,Bt,Ep,Pl,Rt,Mt |
| 23 | Cpx,Nam,Bt,Pa,Ep,Pl,Rt,Mt |
| 24 | Nam,Bt,Chl,Pa,Ep,Pl,Rt,Mt |
| 25 | Cpx,Nam,Bt,Ep,Pl,Rt,Mt |
| 26 | Cpx,Nam,Bt,Ep,Pl,Tit,Mt |
| 27 | Cpx,Bt,Ep,Pl,Tit,Mt |
| 28 | Cpx,Phe,Bt,Ep,Pl,Tit,Mt |
| 29 | Cpx,Bt,Chl,Ep,Pl,Tit,Mt |
| 30 | Cpx,Bt,Pa,Ep,Pl,Tit,Mt |
| 31 | Cpx,Nam,Phe,Bt,Pl,Tit,Mt |
| 32 | Cpx,Nam,Phe,Bt,Ep,Pl,Tit,Mt |
| 33 | Nam,Bt,Pa,Ep,Pl,Rt,Tit,Mt |
| 34 | Cpx,Nam,Bt,Ep,Pl,Rt,Tit,Mt |
| 35 | Cpx,Nam,Phe,Bt,Pl,Rt,Tit,Mt |
| 36 | Bt,Chl,Pl,Rt,Tit,Mt |
| 37 | Cam,Bt,Chl,Pl,Tit,Mt |
| 38 | Cpx,Nam,Phe,Bt,Chl,Pl,Tit,Mt |
| 39 | Cpx,Phe,Nam,Chl,Ep,Pl,Tit,Mt |

Omphacite blueschist 25243

| No. | Assemblage |
|---|---|
| 1 | Amp,Ep,,Bt,Chl,Pl,Qtz,Tit,W |
| 2 | Amp,Ep,Phe,Bt,Chl,Pl,Qtz,Tit,W |
| 3 | Amp,Cpx,Ep,Phe,Chl,Pl,Tit,Qtz |
| 4 | Nam,Amp,Cpx,Ep,Phe,Chl,Pl,Tit,W |
| 5 | Nam,Cpx,Ep,Phe,Chl,Law,Tit,Qtz |
| 6 | Nam,Cpx,Ep,Phe,Chl,Law,Tit |
| 7 | Nam,Cpx,Ep,Phe,Chl,Law,Tit,Rt |
| 8 | Nam,Cpx,Ep,Phe,Chl,Law,Rt |
| 9 | Amp,Ep,Bt,Chl,Pl,Tit,Qtz |
| 10 | Amp,Ep,Phe,Bt,Chl,Pl,Tit,Qtz |
| 11 | Nam,Cpx,Ep,Phe,Chl,Law,Rt,Qtz |
| 12 | Nam,Cpx,Ep,Phe,Chl,Law,Tit,Rt,Qtz |
| 13 | Nam,Cpx,Ep,Phe,Chl,Tit,Rt,Qtz |

Table 6 (*continued*)

Omphacite blueschist 25243

| No. | Assemblage |
|---|---|
| 14 | Amp,Ep,Bt,Chl,Pl,Tit,Mt,Qtz |
| 15 | Amp,Ep,Bt,Pl,Tit,Mt,Qtz |
| 16 | Nam,Amp,Cpx,Ep,Phe,Chl,Tit,Rt,Qtz |
| 17 | Nam,Amp,Cpx,Ep,Phe,Chl,Rt,Qtz |
| 18 | Amp,Cpx,Ep,Phe,Chl,Rt,Qtz |
| 19 | Amp,Cpx,Ep,Phe,Rt,Qtz |
| 20 | Amp,Cpx,Ep,Phe,Rt,Mt,Qtz |
| 21 | Amp,Cpx,Ep,Phe,Chl,Rt,Mt,Qtz |
| 22 | Grt,Amp,Cpx,Ep,Phe,Chl,Rt,Mt,Qtz |
| 23 | Grt,Nam,Cpx,Ep,Phe,Chl,Rt,Qtz |
| 24 | Grt,Amp,Cpx,Ep,Phe,Chl,Rt,Qtz |
| 25 | Grt,Nam,Amp,Cpx,Ep,Phe,Chl,Rt,Qtz |
| 26 | Amp,Cpx,Ep,Phe,Pl,Rt,Qtz |
| 27 | Amp,Cpx,Ep,Phe,Pl,Tit,Rt,Qtz |
| 28 | Amp,Ep,Bt,Chl,Pl,Tit,Rt,Mt,Qtz |
| 29 | Amp,Ep,Phe,Chl,Pl,Tit,Mt,Qtz |
| 30 | Nam,Amp,Ep,Phe,Chl,Tit,Qtz |
| 31 | Amp,Cpx,Ep,Phe,Chl,Tit,Qtz |
| 32 | Amp,Ep,Phe,Chl,Tit,Qtz |
| 33 | Nam,Amp,Ep,Phe,Chl,Pl,Tit,Qtz |
| 34 | Amp,Ep,Bt,Chl,Pl,Tit,Rt,Qtz |
| 35 | Amp,Ep,Phe,Chl,Pl,Tit,Rt,Qtz |
| 36 | Amp,Cpx,Ep,Phe,Chl,Pl,Tit,Rt,Qtz |
| 37 | Amp,Ep,Phe,Chl,Bt,Pl,Tit,Rt,Qtz |
| 38 | Amp,Ep,Phe,Bt,Pl,Tit,Rt,Qtz |
| 39 | Amp,Ep,Bt,Pl,Tit,Rt,Qtz |
| 40 | Amp,Ep,Bt,Pl,Tit,Rt,Mt,Qtz |
| 41 | Amp,Cpx,Ep,Bt,Pl,Tit,Mt,Qtz |
| 42 | Amp,Cpx,Bt,Pl,Tit,Mt,Qtz |
| 43 | Amp,Cpx,Ep,Phe,Chl,Tit,Rt,Qtz |
| 44 | Amp,Cpx,Ep,Phe,Tit,Rt,Qtz |
| 45 | Amp,Cpx,Ep,Phe,Pl,Tit,Rt,Qtz |

Eclogite 25323

| No. | Assemblage |
|---|---|
| 1 | Amp,Cpx,Ep,Phe,Chl,Bt,Pl,Tit,W |
| 2 | Amp,Cpx,Ep,Phe,Chl,Pl,Tit,W |
| 3 | Nam,Amp,Cpx,Ep,Phe,Chl,Pl,Tit,W |
| 4 | Nam,Cpx,Ep,Phe,Chl,Tit,W |
| 5 | Nam,Cpx,Ep,Phe,Chl,Tit,Rt,W |
| 6 | Nam,Amp,Cpx,Ep,Phe,Chl,Tit,Rt,W |
| 7 | Amp,Cpx,Ep,Phe,Chl,Rt,W |
| 8 | Amp,Cpx,Ep,Phe,Rt,Tit,W |
| 9 | Amp,Cpx,Ep,Phe,Tit,W |
| 10 | Amp,Cpx,Ep,Phe,Pl,Tit,W |
| 11 | Amp,Cpx,Ep,Phe,Chl,Tit,W |
| 12 | Nam,Amp,Cpx,Ep,Phe,Pl,Tit,W |
| 13 | Nam,Amp,Cpx,Ep,Phe,Tit,W |
| 14 | Cpx,Phe,Chl,Amp,Ep,Rt,Mt,W |
| 15 | Grt,Cpx,Phe,Chl,Amp,Ep,Rt,Mt,W |
| 16 | Grt,Cpx,Phe,Chl,Amp,Ep,Rt,W |
| 17 | Amp,Cpx,Ep,Phe,Pl,Rt,Mt,W |
| 18 | Amp,Cpx,Ep,Phe,Pl,Rt,W |
| 19 | Amp,Cpx,Ep,Phe,Pl,Rt,Tit,W |
| 20 | Amp,Cpx,Ep,Phe,Pl,Rt,Tit,Mt,W |

(*continued on next page*)

Table 6 (*continued*)

| Eclogite 25323 | |
|---|---|
| No. | Assemblage |
| 21 | Amp,Cpx,Ep,Phe,Pl,Tit,Mt,W |
| 22 | Amp,Cpx,Ep,Phe,Bt,Pl,Tit,Mt,W |
| 23 | Amp,Cpx,Ep,Bt,Pl,Qtz,Tit,W |
| 24 | Amp,Cpx,Ep,Phe,Bt,Pl,Qtz,Tit,W |
| 25 | Amp,Cpx,Ep,Phe,Bt,Pl,Rt,Mt,W |
| 26 | Amp,Cpx,Ep,Phe,Bt,Pl,Tit,W |
| 27 | Amp,Cpx,Ep,Phe,Bt,Pl,Tit,Rt,W |
| 28 | Amp,Cpx,Ep,Phe,Bt,Pl,Rt,W |
| 29 | Amp,Cpx,Ep,Phe,Bt,Pl,Tit,Rt,Mt,W |
| 30 | Amp,Cpx,Ep,Phe,Bt,Pl,Qtz,Tit,Mt,W |
| 31 | Amp,Cpx,Ep,Phe,Bt,Pl,Tit,Rt,Mt,W |
| 32 | Cpx,Phe,Amp,Ep,Qtz,Rt,Mt,W |
| 33 | Amp,Cpx,Ep,Bt,Pl,Qtz,Tit,Mt,W |
| 34 | Amp,Cpx,Ep,Bt,Pl,Kfs,Qtz,Tit,Mt,W |
| 35 | Amp,Cpx,Ep,Bt,Pl,Kfs,Tit,Mt,W |
| 36 | Amp,Cpx,Ep,Bt,Pl,Kfs,Tit,Mt,W |
| 37 | Amp,Cpx,Bt,Pl,Kfs,Tit,Mt,W |
| 38 | Grt,Cpx,Phe,Amp,Ep,Pl,Qtz,Rt,Mt,W |
| 39 | Grt,Nam,Cpx,Phe,Chl,Amp,Ep,Rt,W |
| 40 | Nam,Cpx,Ep,Phe,Chl,Law,Tit,Rt,W |
| 41 | Amp,Cpx,Ep,Phe,Chl,Tit,Rt,W |
| 42 | Cpx,Phe,Amp,Ep,Pl,Rt,Mt,W |
| 43 | Amp,Cpx,Ep,Phe,Rt,Mt,W |
| 44 | Grt,Cpx,Phe,Amp,Ep,Rt,Mt |
| 45 | Grt,Cpx,Phe,Chl,Amp,Ep,Rt,Mt,Qtz,W |
| 46 | Grt,Cpx,Phe,Chl,Amp,Ep,Rt,Mt,Qtz |
| 47 | Amp,Cpx,Ep,Phe,Chl,Rt,Qtz |
| 48 | Amp,Cpx,Ep,Phe,Chl,Rt,Qtz,W |
| 49 | Amp,Cpx,Ep,Phe,Chl,Rt,Mt,Qtz,W |
| 50 | Amp,Cpx,Ep,Phe,Chl,Tit,Rt,Qtz,W |
| 51 | Amp,Cpx,Ep,Phe,Chl,Tit,Rt,Qtz |
| 52 | Amp,Cpx,Ep,Phe,Chl,Tit,Qtz |
| 53 | Amp,Cpx,Ep,Phe,Chl,Tit,Qtz,W |
| 54 | Nam,Amp,Cpx,Ep,Phe,Chl,Tit,Qtz,W |
| 55 | Nam,Amp,Cpx,Ep,Phe,Tit,Qtz,W |
| 56 | Nam,Amp,Cpx,Ep,Phe,Pl,Tit,Qtz,W |
| 57 | Nam,Amp,Cpx,Ep,Phe,Chl,Pl,Tit,Qtz |
| 58 | Nam,Amp,Cpx,Ep,Phe,Chl,Pl,Tit,Qtz,W |

serpentinite mélanges, and have been corroborated from other samples studied by Krebs (2006).

### 2.5. *Geochronology and comprehensive pressure–temperature–time paths*

In order to clarify the interrelationships between the above three types of P–T paths in the same subduction zone, and to allow assessment of subduction- and return-path rates, complementary geochronological techniques were applied to the three key samples reported here. Details of analytical procedures and data reduction are summarized in the Appendix.

Rb–StexSr isochron diagrams for eclogite 25323 (74.7±0.5 Ma), omphacite blueschist 25243 (80.3±1.1 Ma) and jadeite blueschist 25356 (62.1±1.4 Ma) are shown in Fig. 10.

Fig. 11a shows the results of U–Pb analysis of two fractions of zircon yielding ages of 137.8±1.9 Ma and 139.1±3.6 Ma for the protolith of eclogite 25323. The low $^{206}Pb/^{204}Pb$ ratios (see Appendix) suggest that these ages are not reliable, but they are a first bench mark for the age of the initial oceanic crust subducted. For the same rock a seven-point Lu–Hf isochron with omphacite, amphibole, whole-rock, epidote and three grain-size fractions of garnet shown in Fig. 11b indicates an age of 103.6±2.7 Ma. The release spectra for step-heated phengites depicted in Fig. 12 indicate ages of 73.42±0.74 Ma for eclogite 25323 and 73.85±0.79 Ma for omphacite blueschist 25243. All geochronological results are compiled together with the pressure–temperature determinations in Table 2 and shown in Fig. 3.

A key element in constructing the P–T–t paths and in estimating subduction rates and return path rates is the concept of "closure temperatures", i.e. those temperatures at which the isotopic systems studied exhibit critical slowing down for geological time spans. Although critical views and controversial discussion are known from the literature (e.g. Villa, 1998), a multitude of realistic results have also been obtained using this concept (e.g. Parrish et al., 1988; Mezger et al., 1989; Cosca et al., 1991; Gebauer et al., 1997). We accept its validity for the present purpose and see no specific reasons why complicating factors (e.g. Villa, 1998) should arise. For phengite, the closure temperatures used were 500 °C for the Rb–Sr-system (~450°–550 °C, Hawkesworth and van Calsteren, 1992) and 375 °C for Ar–Ar (~350°–400 °C, Hames and Bowring, 1994). For the Lu–Hf system in garnet Scherer et al. (2000) have suggested a similar or even higher temperature for isotopic closure than that established for the corresponding Sm–Nd system. Considering that the closure temperature for Nd diffusion in garnet has been suggested to range between 700°–750 °C (Ganguly et al., 1988), we adopt a closure temperature of 750 °C for Lu–Hf.

Table 2 and Fig. 3 indicate that, as a general feature, the maximum metamorphic temperatures derived for the three samples decrease with decreasing ages from 103.6 to 62.1 Ma. The older P–T–t paths exhibit a flatter ("hotter") subduction gradient, whereas the youngest P–T path is characterized by the steepest ("coldest") gradient during subduction. We suggest that this trend is a logical consequence of the thermal evolution of a young intra-oceanic subduction zone, and summarize the observed P–T–t data as follows (Table 2, Fig. 3):

1) *The oldest, "nascent" stage documented by eclogite* 25323: This stage exhibits typically shallow ("hot")

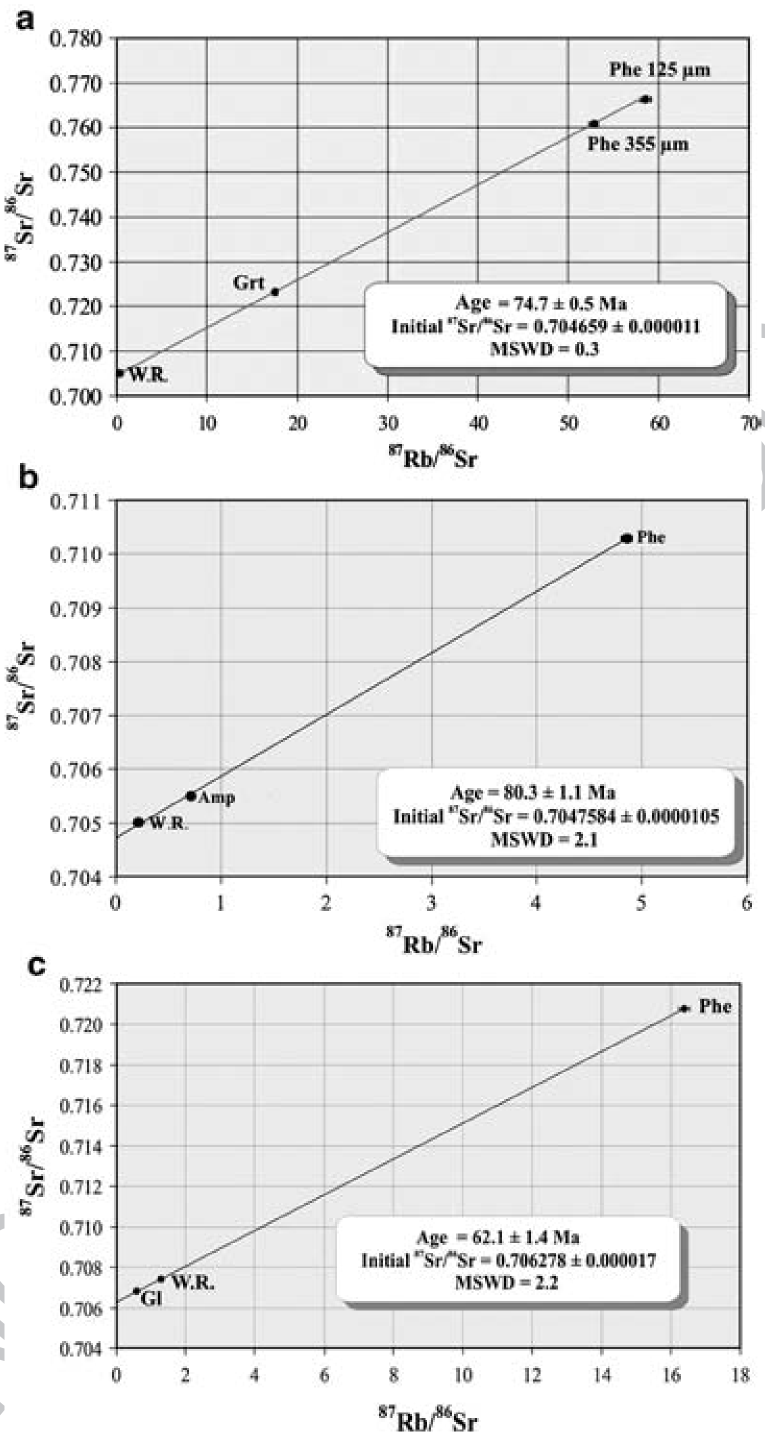


Fig. 10. Rb–Sr isochron diagrams for eclogite 25323 (a), omphacite blueschist 25243 (b) and jadeite blueschist 25356 (c).

P/T-gradients with peak P–T conditions of about 750 °C/23 kbar. This type of anticlockwise path with isobaric cooling and later isothermal return is common to many eclogites studied from the Rio San Juan mélanges. The beginning of subduction is constrained by U–Pb-zircon protolith ages of 139.1 ± 3.6 Ma. This date fits well with regional considerations (Pindell et al., 2005) calling for subduction initiation at about 120 Ma. Maximum metamorphic conditions are recorded by Lu–Hf-data on Grt–Ep–Amp–Omp–

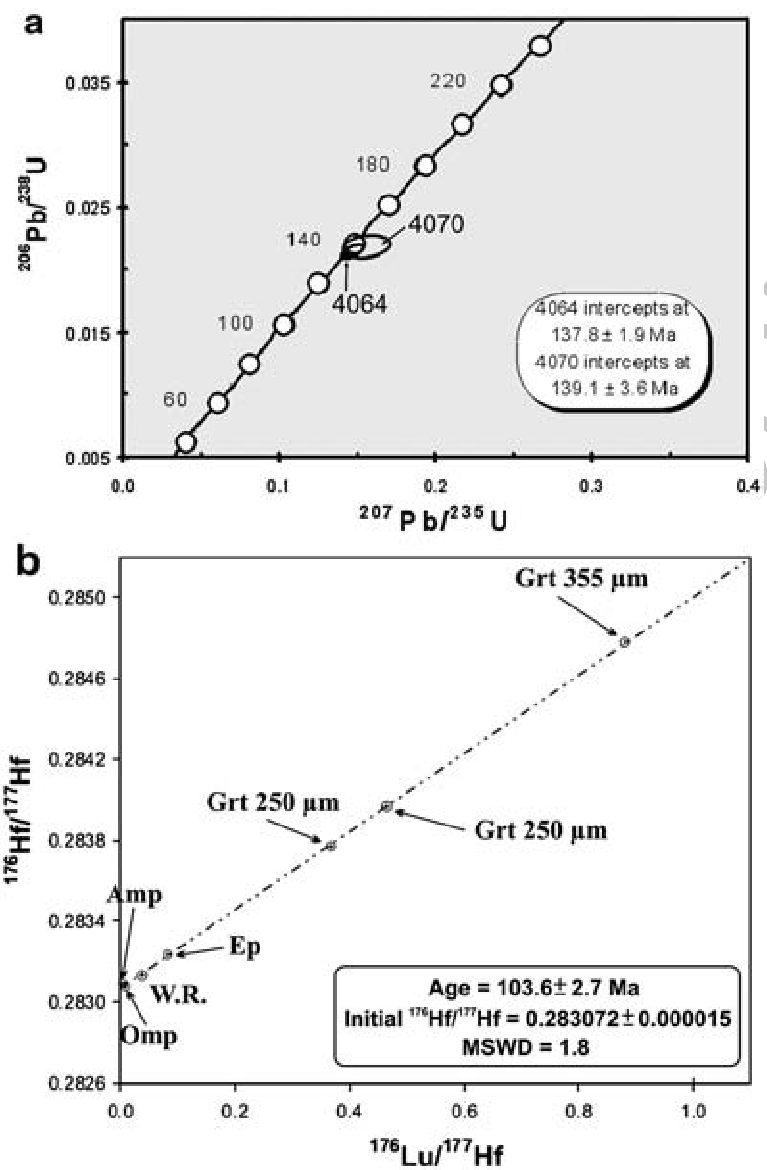


Fig. 11. U–Pb concordia diagram (a) and Lu–Hf-isochron diagram (b) for eclogite 25323.

WR which yield an age of 103.6±2.7 Ma, while Rb–Sr-ages of 74.7±0.5 Ma (Phe–Grt–WR) and Ar–Ar-plateau ages of 73.42±0.74 Ma (Phe) constrain the return path.

2) *Evolving stage as exemplified by omphacite blueschist* 25243: Continuous cooling of the subduction-zone system and steepening of the subduction-zone-related P/T-gradient is indicated by this stage. An age of 80.3±1.1 Ma (Rb–Sr on Phe–Amp–WR) is derived for maximum metamorphic conditions of 520 °C/17 kbar, whereas cooling below 400 °C during return is documented by Ar–Ar-ages on phengite of 73.85±0.79 Ma.

3) *Mature stage as typified by jadeite blueschist* 25356: Very steep ("cold") P/T-gradients (380 °C/18 kbar) are indicated by P–T-data derived from jadeite blueschists. Rb–Sr-ages (Phe–Amp–WR) date peak metamorphic conditions at 62.1±1.4 Ma.

Assuming the closure temperatures discussed above, the P–T–t results summarized in Table 2 can be used to derive information on cooling and exhumation rates, providing data on the material transport within an evolving subduction zone in time and space. *In the following discussion, we follow* Gerya et al. (2002) *and* Gerya and Stöckhert (2002)*, and use the term "exhumation rate" to*

Please cite this article as: Krebs, M., et al., The dynamics of intra-oceanic subduction zones: A direct comparison between fossil petrological evidence (Rio San Juan Complex, Dominican Republic) and numerical simulation, Lithos (2007), doi:10.1016/j.lithos.2007.09.003

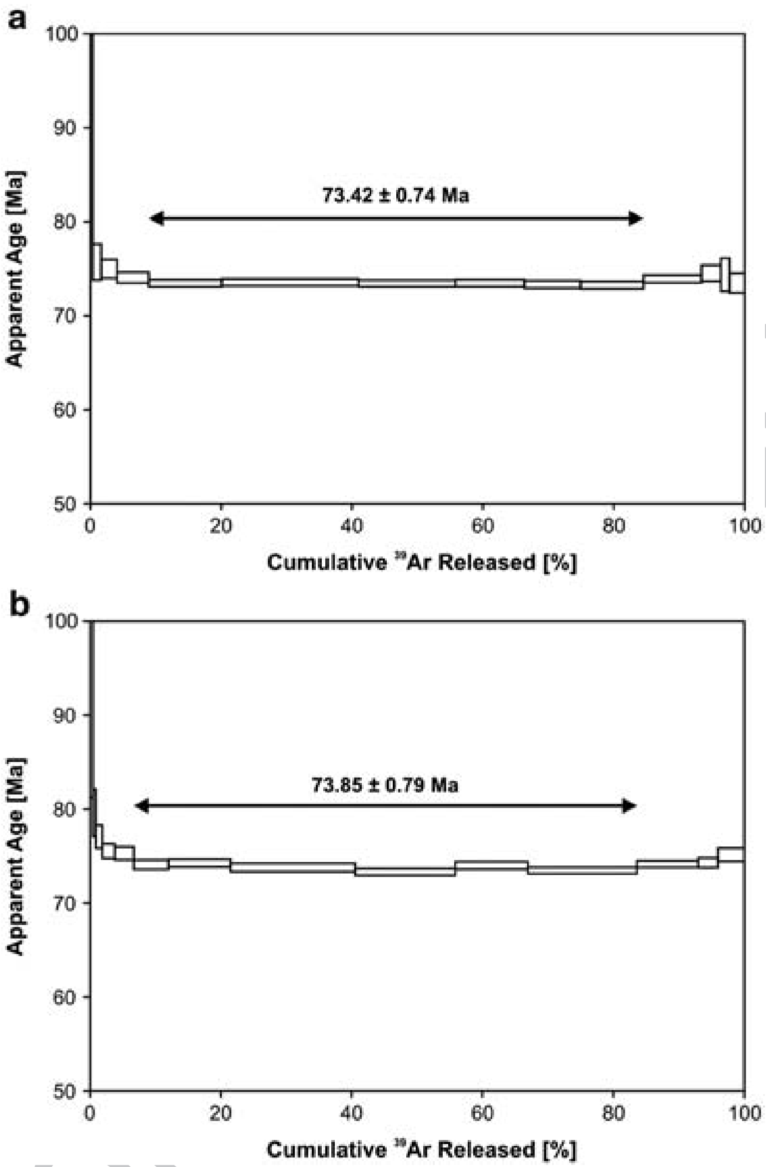


Fig. 12. $^{40}Ar$–$^{39}Ar$ release spectra for step-heated phengites of eclogite 25323 (a) and omphacite blueschist 25243 (b).

*denote the vertical component of the return path.* This rate can easily be obtained from changes of depth (i.e., pressure) with time, regardless of the dynamics and geometry of return flow in the subduction channel. It is also a parameter directly provided by the numerical simulation. We assume that, for most of the duration of subduction, erosion in the fore-arc region is small. No attempt has been made to introduce this variable into the numerical simulation. All cooling/heating rates and burial/exhumation rates derived from the P–T–t paths in Fig. 3 are summarized in Table 7.

For *eclogite* 25323, average cooling and exhumation rates can be derived from the path coordinates for peak metamorphism at 103.6 Ma B(1) and the retrograde stage D(1) at 74.7 Ma / 500 °C. Average cooling rates are 9 °C/Ma with corresponding exhumation rates of 1.2 mm/a. However, the eclogite P–T–t path between the datable coordinates B(1) (Lu–Hf) and D(1) (Rb–Sr) is distinctly discontinuous, with an initially almost isobaric (B(1)–C(1)) and subsequently (C(1)–D(1)) almost isothermal leg. (Table 2, Fig. 3). Assuming an overall cooling rate closer to 7 °C/Ma for the subduction zone, as deduced from the shift between the *omphacite blueschist* and *jadeite blueschist* P–T–t paths (see below) allows the C(1) "corner" to be "dated" at approximately 84 Ma. Thus, an exhumation rate of 4.8 mm/a for the post-(C(1) stage is more realistic than the average of 1.2 mm/a obtained

Table 7
Comparison of elapsed time, cooling/heating and burial/exhumation rates for different legs of the P–T–t-paths of Fig. 9 with results from the numerical simulation

| | | | Elapsed time | Cooling/ heating rate | Burial/ exhumation rate |
|---|---|---|---|---|---|
| *Eclogite* | | | | | |
| Pre-B | Observed | | <36 Ma | | |
| (1) | Modeled | 10 mm/a | 19.2 Ma | 37 °C/Ma | 3.6 mm/a |
| | | 20 mm/a | 9.6 Ma | 74 °C/Ma | 7.3 mm/a |
| | | 30 mm/a | 6.4 Ma | 112 °C/Ma | 11 mm/a |
| | | 40 mm/a | 4.8 Ma | 149 °C/Ma | 14.5 mm/a |
| B(1)– | Observed | | 20.9 Ma | 9 °C/Ma | 0.17 mm/a |
| C(1) | modeled | 10 mm/a | 22.5 Ma | 8 °C/Ma | – |
| | | 20 mm/a | 11.3 Ma | 16 °C/Ma | – |
| | | 30 mm/a | 7.5 Ma | 24 °C/Ma | – |
| | | 40 mm/a | 5.6 Ma | 33 °C/Ma | – |
| B(1)– | Observed | | 29.2 Ma | 9 °C/Ma | 1.2 mm/a |
| D(1) | Modeled | 10 mm/a | 47.1 Ma | 7 °C/Ma | 0.5 mm/a |
| | | 20 mm/a | 24.6 Ma | 13 °C/Ma | 0.9 mm/a |
| | | 30 mm/a | 15.7 Ma | 21 °C/Ma | 1.4 mm/a |
| | | 40 mm/a | 11.7 Ma | 28 °C/Ma | 2.0 mm/a |
| C(1)– | Observed | | 8.3 Ma | 7 °C/Ma | 4.8 mm/a |
| D(1) | Modeled | 10 mm/a | 16.5 Ma | 9 °C/Ma | 1.8 mm/a |
| | | 20 mm/a | 8.3 Ma | 18 °C/Ma | 3.6 mm/a |
| | | 30 mm/a | 5.5 Ma | 27 °C/Ma | 5.4 mm/a |
| | | 40 mm/a | 4.1 Ma | 36 °C/Ma | 7.3 mm/a |
| D(1)– | Observed | | 1.3 Ma | 96 °C/Ma | 15.2 mm/a |
| E(1) | Modeled | 10 mm/a | 7.8 Ma | 19 °C/Ma | 2.5 mm/a |
| | | 20 mm/a | 3.9 Ma | 38 °C/Ma | 5.1 mm/a |
| | | 30 mm/a | 2.6 Ma | 58 °C/Ma | 7.6 mm/a |
| | | 40 mm/a | 1.9 Ma | 76 °C/Ma | 10.2 mm/a |
| C(1)– | Observed | | 9.6 Ma | 20 °C/Ma | 5.5 mm/a |
| E(1) | Modeled | 10 mm/a | 24.3 Ma | 11 °C/Ma | 3.1 mm/a |
| | | 20 mm/a | 12.2 Ma | 20 °C/Ma | 4.1 mm/a |
| | | 30 mm/a | 8.1 Ma | 31 °C/Ma | 6.2 mm/a |
| | | 40 mm/a | 6.1 Ma | 44 °C/Ma | 12.3 mm/a |
| | | | | | |
| *Omphacite blueschist* | | | | | |
| Pre- | Observed | | <24 Ma | | |
| B(2) | Modeled | 10 mm/a | 10.3 Ma | 37 °C/Ma | 5.7 mm/a |
| | | 20 mm/a | 5.1 Ma | 73 °C/Ma | 11.4 mm/a |
| | | 30 mm/a | 3.4 Ma | 110 °C/Ma | 17.1 mm/a |
| | | 40 mm/a | 2.6 Ma | 147 °C/Ma | 22.8 mm/a |
| B(2)– | Observed | | 6.4 Ma | 20 °C/Ma | 5.7 mm/a |
| D(2) | Modeled | 10 mm/a | 16.2 Ma | 11 °C/Ma | 2.0 mm/a |
| | | 20 mm/a | 8.1 Ma | 21 °C/Ma | 4.1 mm/a |
| | | 30 mm/a | 5.4 Ma | 32 °C/Ma | 6.1 mm/a |
| | | 40 mm/a | 4.1 Ma | 43 °C/Ma | 8.2 mm/a |

Changes in these parameters with different assumed convergence rates in the model allow the "paleo-convergence rates" of the Rio San Juan subduction zone to be estimated.

above. Since the Rb–Sr- and Ar–Ar-ages are very close to each other, with almost overlapping error ranges, it is difficult to make definitive statements for cooling and exhumation rates during the latest stages of the eclogite P–T–t path. Nevertheless, at shallow post-D(1) levels both cooling and exhumation rates do appear to increase sharply, with calculated, but probably unrealistically high values of c. 96 °C/Ma and 15.2 mm/a, respectively. Averaging the entire exhumation leg after C(1) leads to 5.5 mm/a and 20 °C/Ma.

The peak-metamorphic conditions experienced by *omphacite blueschist* 25243 (80.3 Ma) are reached 23 Ma later than for the eclogite and document a distinctive change in the thermal structure within the evolving subduction zone. The calculated cooling rate is 20 °C/Ma and the exhumation rate is c. 5.7 mm/a. For *jadeite blueschist* 25356 only one age for the peak of metamorphism is available (62.1 Ma). Thus, no exhumation rates can be calculated directly. However, these data nicely document the continuous cooling of the maturing subduction zone. As the peak pressure conditions for both the omphacite blueschist and the jadeite blueschist are nearly identical (ca. 18 kbar), the temperature difference between these stages (which is in the range of 120 °C) marks the cooling of the subduction zone within a time frame of 18 Ma — leading to the value of 7–8 °C/Ma used in the estimate for *eclogite* 25323 above.

## 3. The numerical model

The pressure–temperature–time paths of Fig. 3 can be directly compared to the numerical simulations of intra-oceanic subduction zones presented by Gerya et al. (2002). The design of this numerical model and its implementation for the study of subduction processes in general have been described in considerable detail elsewhere (Gerya et al., 2002, 2004; Gerya and Yuen, 2003a,b; Gerya and Stöckhert, 2005; Stöckhert and Gerya, 2005; Perchuk and Gerya, 2005; Maresch and Gerya, 2005). The simulation uses a regional 2-D model that takes into account the process of hydration of the mantle wedge by the fluid released from a kinematically specified subducting plate (e.g., Gerya et al., 2002, 2004; Gerya and Yuen, 2003a), and specified viscous rheologies to take into account variations in lithology, temperature and strain rate in the subduction zone structure. The kinematic boundary conditions correspond to the corner flow model (e.g., Gerya and Yuen, 2003a). The requisite equations of momentum, continuity and temperature are solved employing the 2-D thermomechanical code I2VIS based on finite differences and marker-in-cell technique (Gerya et al., 2000; Gerya and Yuen, 2003b). A detailed description of the numerical method as well as algorithmic tests are provided by Gerya and Yuen (2003b). A key feature of the Gerya et al. (2002) numerical approach is that pressure–temperature–time paths are easily visualized and interactive comparison between the numerical simulation and P–T–t paths derived from petrological study is possible.



Please cite this article as: Krebs, M., et al., The dynamics of intra-oceanic subduction zones: A direct comparison between fossil petrological evidence (Rio San Juan Complex, Dominican Republic) and numerical simulation, Lithos (2007), doi:10.1016/j.lithos.2007.09.003

Critical input for a numerical model of the fossil Rio San Juan subduction zone is 1) age of the oceanic crust involved, 2) convergence rate and 3) slab dip. We therefore base our comparison on the simulation obtained by Gerya et al. (2002) for their Model A (see Table 1 of Gerya et al., 2002). The critical input parameters for this model are 40 Ma age of the lithosphere for the colliding plates, 30 mm/yr convergence rate and 45° subduction angle.

Pindell et al. (2005) have recently provided an exhaustive summary on the regional development of the Caribbean, in which the current majority view is reviewed and successfully compared with existing regional data. In this model, North and South America began to rift apart in latest Jurassic time. A trench–trench–ridge triple junction must have formed at the western end of the "Proto-Caribbean" gap. The subduction zone along the western continental margin of the Americas must have lengthened at this triple junction to produce an intra-oceanic system bridging this widening gap. The model postulates that at c. 120 Ma this intra-oceanic subduction zone changed polarity and swept eastwards as the so-called Great Arc (Burke, 1988) already described above. The Rio San Juan subduction system, as part of the "Great Arc", thus consumed young oceanic crust, no older than latest Jurassic. The reconstructions of Pindell and Kennan (2001) suggest that at the onset of subduction the age of the crust may have been 20 Ma or less for the Rio San Juan segment, but that 40 Ma is a fitting long-term average for the numerical simulation. For simplicity, we have also chosen the same lithospheric age of 40 Ma for the overriding plate.

Regional considerations of eastward progress of the Great Arc (Pindell and Kennan, 2001; Pindell et al., 2005; see also Fig. 1 in Maresch and Gerya, 2005) suggest low convergence rates at the Rio San Juan subduction zone of 20–40 mm/yr, with a long-term average of c. 22 mm/a (Pindell, pers. communication, 2006). Given the systematic proportionalities between convergence rates on the one hand and burial/exhumation rates as well as heating/cooling rates on the other (Gerya et al., 2002), it is possible to recalculate the results of Model A of Gerya et al. (2002) for convergence rates between 10 and 40 mm/yr (Gerya, pers. commun, 2006). The results are summarized in Table 7.

The basic situation of converging, similarly structured plates makes the choice of a slab dip of 45° reasonable for shallow levels, in accordance with the critical bending radius of oceanic lithosphere of about 200 km. For a slab age of 40 Ma, the expected rate of slab roll-back will be low and comparable to the low convergence rates expected (Pindell, pers. commun. 2003). Thus a stable slab–dip situation to 70 km depth appears reasonable.

## 4. Discussion

The results of the numerical simulations summarized in Fig. 13 and Table 7 show that the array of P–T–t paths derived from the blocks in the Rio San Juan serpentinite mélanges fits the predicted flow patterns, temperature fields and timescales of the numerical simulation very well. On the one hand, this shows that the simulation technique (Gerya et al., 2000; Gerya and Yuen, 2003b) applied to subduction zones (Gerya et al., 2002, Gerya and Stöckhert, 2002) provides a realistic description of this geodynamic process. In particular, strong support for the existence of forced flow in a subduction channel involving hydrated, serpentinized parts of the overlying mantle wedge is provided. On the other hand, the simulation also allows clarification and quantification of the parameters controlling the subduction process of this part of the Great Arc of the Caribbean during the mid-Cretaceous to Early Tertiary.

During the early, the *"nascent"* stage (Fig. 13; 0.8 to 13.9 Ma time panels), no return flow from depths exceeding c. 20 km develops. Samples of subducted material (black rectangle in Fig. 13) experience a prograde evolution to about 750 °C and 23 kbar along a low P/T gradient. A characteristic feature observed in simulations of the initial stages of such a developing subduction zone (see also Gerya et al., 2002) is the discontinuous circulation of material. Subducted to peak conditions, such material (black rectangle Fig. 13) is initially accreted to the almost unhydrated hanging-wall at depth. Continuing displacement of the isotherms to greater depths causes near-isobaric cooling. At a later stage the accreted sample can be set free by hydration and weakening of the mantle wedge, and can return to the surface. This characteristic anticlockwise P–T path is also shown by *eclogite* 25323 of the present study. The excellent agreement between the maximum temperature of c. 750 °C obtained both from petrology and from the simulation represents corroborative evidence for the choice of lithospheric age and slab dip in the model, both of which can change this value. The systematics of the modeling presented by Gerya et al. (2002, pers. communication, 2006) show that at this depth the effect of a younger lithospheric age (c. 3 °C per 1 Ma) could be compensated by a shallower subduction angle (c. 13 °C per degree of dip). However, such exact compensation appears fortuitous. The effect of such changes in age and dip on the exhumation/cooling rates discussed below cannot be quantified from these systematics alone and would have to be tested in a series if further simulations.

The comparison in Table 7 of cooling and exhumation rates, as well as elapsed time between the P–T coordinates of Fig. 3, in general indicates very good and

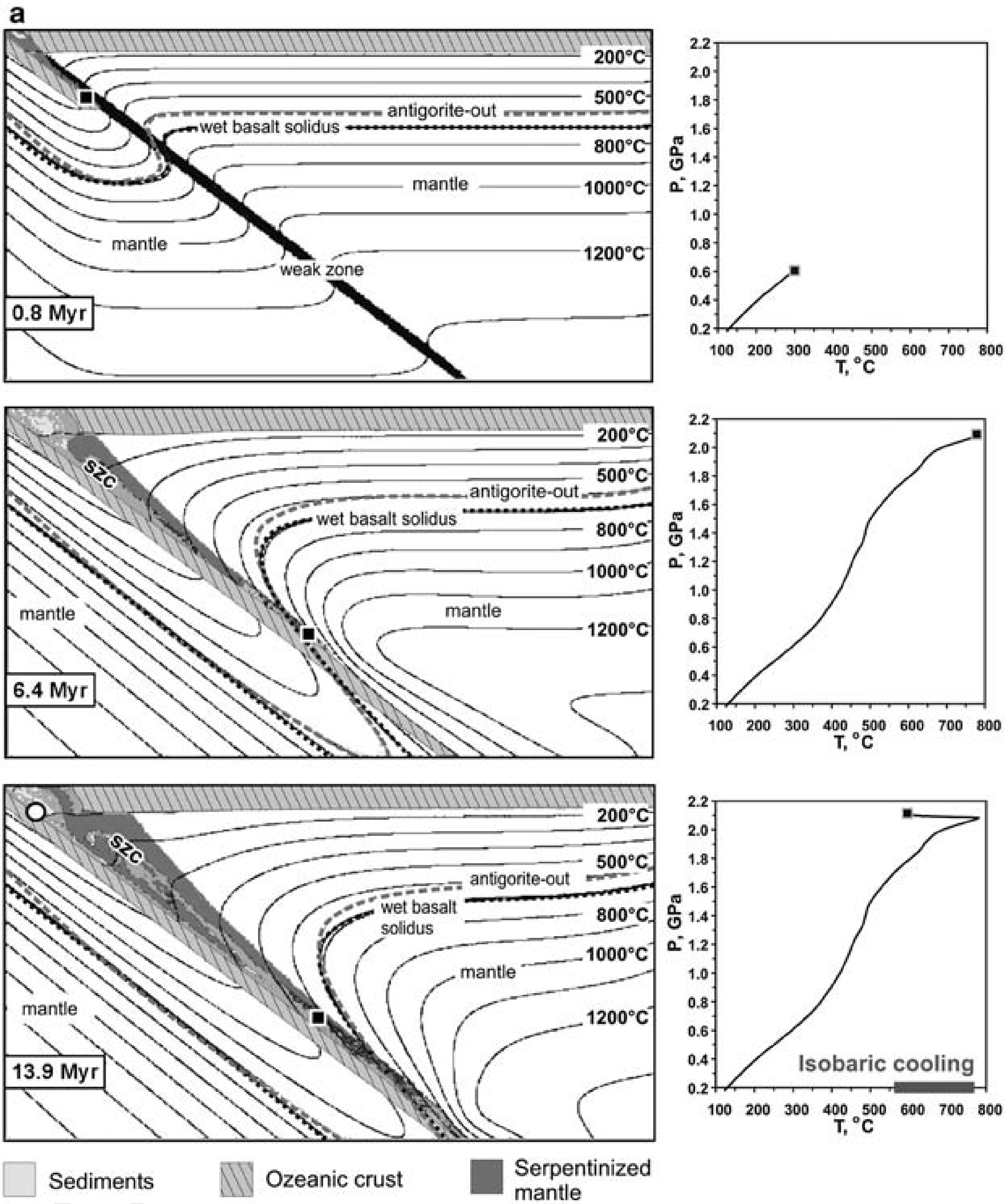


Fig. 13. Variation in time of the geometry and thermal structure (left panel) of a subduction zone with a convergence rate of 30 mm/a, an inclination of the slab of 45° and an assumed age of 40 Ma for both lithospheric plates. Numerical simulation from Gerya et al. (2002; their model A). Three different samples of subducted material (black rectangle, white circle, white star) experience contrasting P–T-evolutions (right panel). SZC Subductionzone channel: Mixture of subducted sediment, oceanic crust (mainly basaltic but also gabbroic crust) and serpentinized mantle. For further explanation see text. Panels provided by Gerya (pers. communication, 2006).

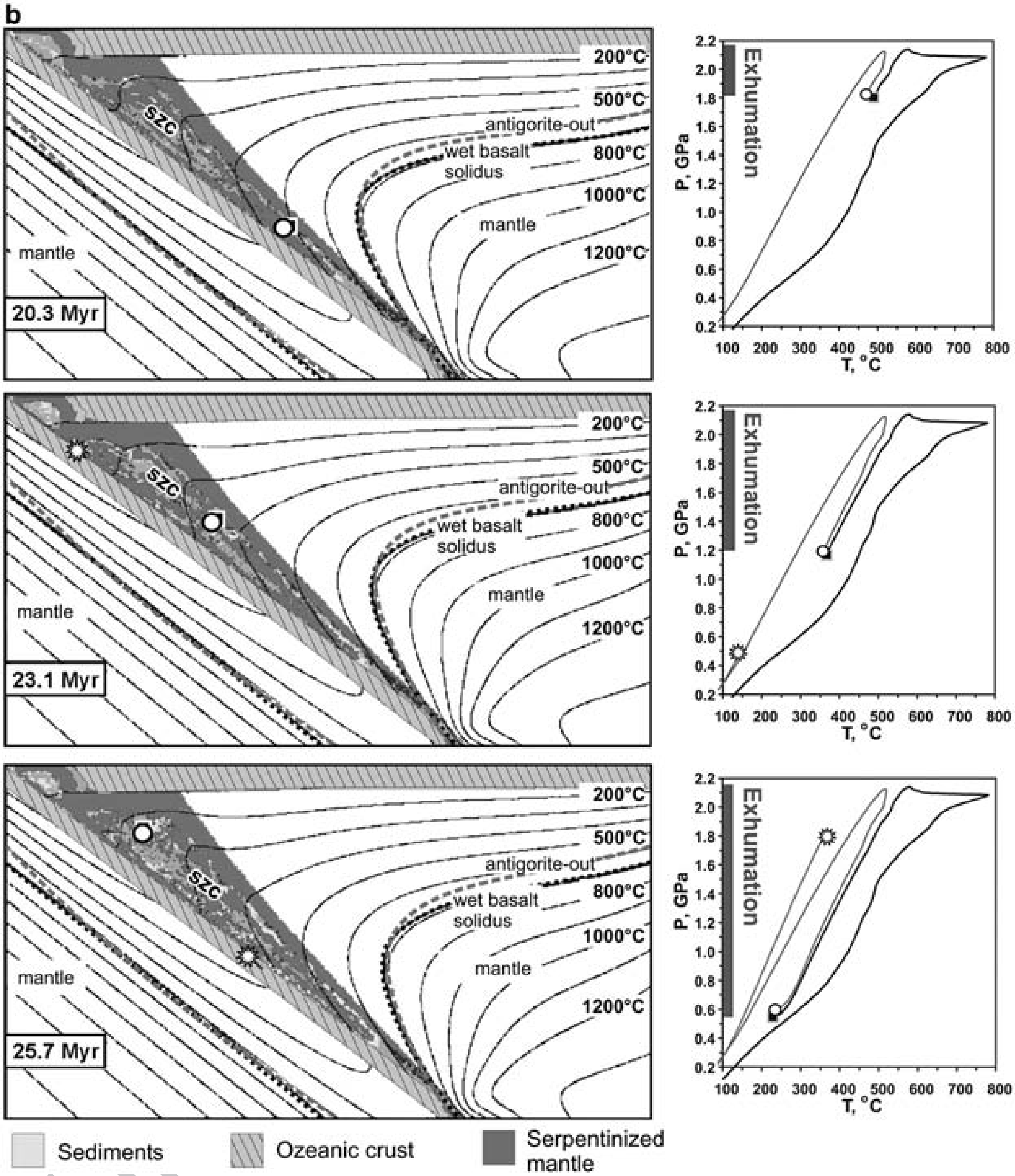


Fig. 13 (*continued*).

consistent agreement between the numerical simulation and the P–T–t paths derived from blocks in the RSJC serpentinite mélange. The difference in the Rb–Sr age defining the D(1) coordinate and the Ar–Ar age defining the E(1) coordinate is very small, so that the D(1)–E(1) leg is poorly defined, and the D(1)–E(1) rates appear unrealistically high. With this exception, the overall picture that emerges is that the early observed rates, i.e. for B(1)–C(1) and B(1)–D(1), are close to modeled rates obtained with convergence rates of 10–15 and 15–25 mm/a, respectively. The later (i.e. C(1)–E(1)) fits simulations with 20–30 mm/a convergence rates.

The initial convergence rate suggested for eclogite 25323 is critical in pinning down the age of initiation of the subduction zone. If an elapsed time of 20 Ma is accepted for the pre-B(1) path from comparison with the simulation, then an age of c. 124 Myr is a minimum for the age of intitiation of the subduction zone.

During the evolving stage (Fig. 13), fragments of subducted material experience continuous circulation in the widening hydrated mantle wedge and samples (white circle in Fig. 13) now record clockwise P–T paths. Continuous cooling and steepening of the subduction-zone P–T gradient is recorded in the subducted material of this stage. The exhumation and cooling rates of the B(2)–D(2) leg of *omphacite blueschist* 25243 (Fig. 3; Table 7) suggest convergence rates of 20–30 mm/a, in accordance with the later stages of the eclogite path.

The late "mature" stage (Fig. 13) is characterized by intense hydration of the mantle wedge and intense return flow from greater depth. In this stage a steady-state thermal configuration is reached and the isotherms are displaced to greatest depth. As seen in Fig. 13 (white star), material subducted during the mature stage records the steepest P/T-gradient and coolest peak conditions. Although no exhumation or cooling rates can be calculated from the P–T–t path of *jadeite blueschist* 25357, the calculated metamorphic peak conditions and the correlated Rb–Sr age of 62.1 Ma give insight into the mature thermal structure of the subduction zone. Temperatures lower than 400 °C at a depth of about 60 km (corresponding to a pressure of ca. 18 kbar) agree well with the thermal structure of the numerical simulation.

Conglomerates of the lower Imbert Formation (Paleocene to lower Eocene, or 50–55 Ma; see Nagle, 1966) contain fragments of serpentinite and metamorphic rocks (Pindell and Draper, 1991), indicating that the mélanges may have reached the surface by this time. As the collision of the Antillean arc with the Bahamas was oblique, it is likely that these deposits were derived from west of the present day Rio San Juan Complex exposure. Unfortunately, the occurrence of these clasts does not necessarily constrain the end of subduction. The mélanges could have been unroofed by erosion during on-going subduction, or, perhaps more likely, they may represent fore-arc mud volcano deposits of the type described by Fryer et al. (1999). Indeed, if exhumation rates of 5–6 mm/a and cooling rates of c. 20 °C/Ma are assumed (Table 7), as suggested by the P–T–t paths of eclogite and omphacite blueschist, then active subduction to 50–45 Ma (Early Eocene) appears realistic.

In combination with the results of the numerical simulation, the P–T–t-data of the Rio San Juan samples yield important insight into the evolution of the Antillean arc that entered the Caribbean gap from the Pacific (Burke et al., 1978; Pindell and Dewey, 1982; Burke et al., 1984; Burke, 1988; Pindell, 1990; Pindell et al., 2005). This began with the development of a west-dipping Benioff zone in Cretaceous time between Central America and the northern Andes, which is the origin of most Caribbean high-pressure metamorphic complexes. Our results constrain the onset of subduction in the Rio San Juan segment of the Great Arc to approximately 120 Ma. This segment was obviously active for more than 70 Ma, which implies that at an assumed average rate of 20 mm/a convergence, a minimum amount of 1400 km of oceanic crust must have been subducted. If plate collision was oblique, then this amount must have been correspondingly higher.

The onset of west-dipping subduction at 120 Ma suggested from this study is completely in accord with an estimate derived by Pindell et al. (2005) from regional considerations. In addition, if the regional reconstructions of Pindell and Kennan (2001) are viewed in a mantle reference frame, an average *orthogonal* convergence rate of 22 mm/a of this part of the Great Caribbean Arc is indicated (Pindell, pers. communication, 2006) between 119 and 46 Ma. Thus three very different lines of evidence – P–T–t-paths of metamorphic rocks, numerical simulation and regional paleogeographic modeling – provide a consistent, comprehensive scenario of the subduction-zone processes of the Caribbean Great Arc in the Greater Antilles.

Another important aspect of this long subduction process is the broad spectrum of different P–T paths and peak conditions recorded by material subducted at different periods of time, as the subduction zone evolved and matured. Indeed, the jadeitites and eclogites exposed in Guatemala (Harlow, 1994; Harlow et al., 2003; Sisson et al., 2003) need not necessarily be the product of two discrete belts of high-pressure/low-temperature rocks formed during two discrete events. As indicated in this study, both types of high-pressure rock can originate in the same evolving, long-lived subduction zone.

## 5. Uncited references Q6

Scherer et al., 2001
Will and Powell, 1992

## Acknowledgements

This work was financially supported by Deutsche Forschungsgemeinschaft (DFG), project SCHE 517/3-1 and 3-2. G. Draper also acknowledges grants from the US National Science Foundation (EAR 83061452 and EAR 8509542) and Latin American-Caribbean Center of Florida International University which funded earlier investigations in the RSJC. Thanks are due to H. Baier, U. Lange, M. Lagos, E. Scherer, M. Bröcker, K. Mezger (Münster) for laboratory assistance, help and discussions and to H. Baier for support with the mass spectrometer. H.-J. Bernhardt (Bochum) provided electron microprobe facilities. We are also indebted to R. Lehmann (Bochum) for skilled work on the figures. This paper was considerably improved by the careful reviews of A. Perchuk and S. Guillot. We also wish to acknowledge T. Gerya for help with calculations and valuable discussions.

## Appendix A. Electron microprobe analyses

Mineral analyses were performed with a Cameca S×50 electron microprobe at the University of Bochum, Germany. The acceleration voltage was 15 kV, the beam current 15–20 nA, the beam diameter 2–5 µm and the counting interval 20 seconds per element. The following standards were used: synthetic pyrope [Si, Al, Mg], rutile [Ti], glass of andradite composition [Fe, Ca], jadeite [Na], K-bearing glass [K], topaz [F], $Cr_2O_3$ [Cr], Ba-silicate glass [Ba(Lα)]. The PAP procedure was applied for matrix correction. Analyses and structural formulae of minerals used for the PT-calculations reported in this paper are given in Table A1. Cation proportions are normalized on the basis of 11 oxygens (mica), 14 oxygens (chlorite), 23 oxygens (amphibole), 6 oxygens (pyroxene), 13 oxygens (epidote) and 12 oxygens (garnet). $Fe_{total}$ is assumed to be $Fe^{2+}$ for mica, chlorite and $Fe^{3+}$ for epidote. $Fe^{2+}/Fe^{3+}$ ratios are calculated on the basis of the following constraints: 46 valences and the sum of cations without Ca, Na and K equal to 13 for amphibole; 24 valences and the sum of cations equal to 8 for garnet; 12 valences and the sum of cations equal to 4 for pyroxene.

## Activity models

The activity models used for standard thermodynamic calculations are summarized in Table 2. In addition, the following approaches were used in pseudosection calculations to describe amphibole solid solutions:*Calcic Amphibole:* Symmetric mixing and DQF models are used for an amphibole with the following five end-members:

Pargasite (parg) $[Na]^{A}[Ca]_2^{M4}[Mg]_3^{M1,3}[Al]_2^{M_2}[Al]_2^{T1}[Si]_2^{T1}[Si]_4^{T2}O_{22}(OH)_2$

Glaucophane (gl) $[0]^{A}[Na]_2^{M4}[Mg]_3^{M1,3}[Al]_2^{M_2}[Si]_4^{T1}[Si]_4^{T2}O_{22}(OH)_2$

Tschermakite (ts) $[0]^{A}[Ca]_2^{M4}[Mg]_3^{M1,3}[Al]_2^{M_2}[Al]_2^{T1}[Si]_2^{T1}[Si]_4^{T2}O_{22}(OH)_2$

Tremolite (tr) $[0]^{A}[Ca]_2^{M4}[Mg]_3^{M1,3}[Mg]_2^{M_2}[Si]_4^{T1}[Si]_4^{T2}O_{22}(OH)_2$

Ferroactinolite (fact) $[0]^{A}[Ca]_2^{M4}[Fe]_3^{M1,3}[Fe]_2^{M_2}[Si]_4^{T1}[Si]_4^{T2}O_{22}(OH)_2$

The ideal activity model used for these amphibole end-members is simple ideal mixing on sites, in which the entropy contribution from the tetrahedral sites is taken as half its configurational value (Holland and Powell, 1998a). Interaction parameters for these end-members are $W_{tr-ts}=20$ kJ/mol, $W_{tr-parg}=44$ kJ/mol, $W_{parg-ts}=-24$ kJ/mol (Powell and Holland, 1999) $W_{fact-tr}=0$ kJ/mol (determined from the data of Okamoto and Toriumi, 2001) and $W_{fact-parg}=38$ kJ/mol (Wei et al., 2003). DQF values of $I_{parg}=40$ kJ/mol (Carson et al., 1999) and $I_{gl}=(77–2.25*P)$ kJ/mol (Carson et al., 2000) are derived from matching calculated "A site" and "M4 site" Na with that observed in natural minerals.

*Sodic Amphibole*: Ideal mixing and DQF models are used for a quaternary sodic amphibole solution according to Will et al. (1998). Instead of hornblende, the end-member tschermakite is introduced. The DQF parameter $I_{ts}=21.18$ kJ/mol for the non-ideal substitution of tschermakite is calculated as outlined in Will (1992). Q3

Lawsonite (Lws), Quartz (Qtz), Titanite (Tit), Rutile (Rt), Magnetite (Mt) are taken to be simple end-member minerals with unit activities.

## Geochronological methods

Rock and mineral separation was carried out at the Westfälische Wilhelms-Universität at Münster (Zentrallabor für Geochronologie), Germany. Rock samples were crushed using a jaw-crusher and disk mill (mineral separates) or tungsten carbide mill (whole-rock powders). Different minerals were separated (grain-sizes 355–125 µm) and purified by hand-picking. Rb–Sr, Lu–Hf, and U–Pb isotope analyses were performed at Münster, Ar–Ar-isotope studies at the Geochronology Laboratory of Lehigh University, USA.

For the Rb–Sr analyses, sample quantities between 8 and 40 mg of white mica, amphibole, and garnet as well as between 50 to 70 mg of whole-rock powder were spiked with a suitable $^{87}Rb/^{84}Sr$ mixed spike and subsequently digested in Teflon screw-top vials with a mixture of $HF/HNO_3$ (5:1) on a hot plate. Chemical separation of Rb and Sr and mass-spectrometric analyses were performed as described by Lange et al. (2002).

Rb was measured on a Teledyne SS1290 thermal ionization mass spectrometer, whereas Sr was measured on a VG SECTOR 54 multicollector thermal ionization mass spectrometer. Strontium isotope ratios were normalized to $^{86}Sr/^{88}Sr$ ratio of 0.1194. Measured Rb



Please cite this article as: Krebs, M., et al., The dynamics of intra-oceanic subduction zones: A direct comparison between fossil petrological evidence (Rio San Juan Complex, Dominican Republic) and numerical simulation, Lithos (2007), doi:10.1016/j.lithos.2007.09.003

ratios were corrected for mass fractionation using a factor deduced from multiple measurements of the Rb standard NBS 607. Total procedural blanks were less than 0.1 ng for Rb and 0.15 ng for Sr, respectively. Based on repeated measurements, the $^{87}Rb/^{86}Sr$ ratios were assigned an uncertainty of ±1% (2$\sigma$). Repeated measurements of the NBS 987 standard gave an average $^{87}Sr/^{86}Sr$ ratio of 0.710307±16 (2$\sigma$, $n$=23). The Rb–Sr isotope data are summarised in Table A3. All Rb–Sr ages were calculated using the constants recommended by the IUGS and the least squares regression technique of York (1969). Ages and errors are reported at the 2$\sigma$ level.

Carefully handpicked mineral separates of garnet, omphacite, epidote, amphibole and a whole-rock separate were used for Lu–Hf analyses. The samples (35–50 mg garnet, 15–30 mg omphacite, amphibole, epidote) were washed for 15 min in cold 2.5 M HCl and rinsed with distilled water. As for a split of 50 mg whole-rock powder these samples were spiked with a $^{180}Hf/^{176}Lu$ mixed spike and digested in Savillex vials placed inside Parr Teflon bombs at 180 °C using HF/$HClO_4$. A matrix-independent, one-column separation procedure for Lu and Hf was used (Münker et al., 2001). Lutetium and Hf were analysed in static mode on the Micromass Isoprobe. Measured Hf isotope ratios was corrected for mass bias using $^{179}Hf/^{177}Hf$=0.7325 and the exponential law. Admixed Re was used to apply an external mass bias correction to the Lu isotope dilution measurements. Measured $^{176}Hf/^{177}Hf$ values are reported relative to a $^{176}Hf/^{177}Hf$ of 0.282160 for the Münster Ames Hf standard that is isotopically indistinguishable from the JMC 475 standard. External reproducibility for $^{176}Hf/^{177}Hf$ is±50 ppm. Procedural blanks for Lu and Hf were 10 pg and 50 pg respectively. Isotope ratios are listed in Table A4. The calculated age of the seven-point omphacite–amphibole–whole-rock-epidote–garnet(three separates) isochron and the initial isotope composition are based on the $^{176}Lu$ decay constant calibrated by Scherer (2001). The external $^{176}Lu/^{177}Hf$ 2$\sigma$ error is 1%. Regressions were calculated using the Isoplot/Ex program, version 2.49 (Ludwig, 2001).

Rare zircons of eclogite were used for the isotopic analyses of U and Pb. Two fractions of the least corroded and inclusion-poor grains were air-abraded (Krogh, 1982). The abraded grains were spiked with a mixed $^{208}Pb/^{235}U$ tracer before dissolution and digested in a 3 ml Teflon vial inside Krogh-style Teflon bombs using 24 N HF. Chemical extraction of U and Pb were carried out by procedures similar to those described by Krogh (1973). U and Pb were loaded with phosphoric acid and silica gel on single Re filaments and measured on a VG Sector 54 multicollector mass spectrometer. Total procedural blanks were less than 30 pg for Pb and 6 pg for U. Isotope ratios of U and Pb were corrected for mass discrimination with a factor of 0.11% per a.m.u., based on analyses of standards (NBS-SRM U-500 and NBS-SRM 982). For initial lead correction, isotopic compositions were calculated according to the model of Stacey and Kramers (1975). All ages and error ellipses were calculated using the Isoplot program, version 2.49 (Ludwig, 1991), which uses IUGS recommended decay constants (Steiger and Jäger, 1977). Isotope ratios and corresponding apparent ages are given in Table A5.

For the Ar–Ar analyses, phengite separates from eclogite 25323 and omphacite blueschist 25243 were packaged in Cu foil and sealed in evacuated quartz vials. Packets containing GA1550 biotite (97.9 Ma; McDougall and Roksandic, 1974) were spaced evenly throughout the vials to monitor the neutron flux during irradiation. $CaF_2$ and $K_2SO_4$ were also included in the irradiation package to determine neutron-induced interferences from Ca and K, respectively. The samples were irradiated for 5 h in the 5C position of the research reactor at McMaster University, Canada.

Argon was extracted from the samples by stepwise heating in a double-vacuum resistance furnace. Argon analyses were performed with a fully automated VG3600 noble gas mass spectrometer equipped with an electron multiplier operated in the analog mode. The mass spectrometer sensitivity was $\sim 6\times10^{-17}$ mol/mV $^{40}Ar$. Extraction line blanks were typically $\sim 3\times10^{-15}$ mol $^{40}Ar$ at 1350 °C and $<1\times10^{-15}$ mol $^{40}Ar$ at temperatures below 1000 °C, and were approximately atmospheric in composition. The isotopic data were corrected for extrac>tion line blank, mass spectrometer background, mass discrimination, radioactive decay of $^{37}Ar$ and $^{39}Ar$, neutron-induced interferences, and atmospheric contaminationprior to calculation of the ages. The interference corrections were: $(^{36}Ar/^{37}Ar)_{Ca}=0.000261$, $(^{39}Ar/^{37}Ar)_{Ca}=0.000680$, and $(^{40}Ar/^{39}Ar)_K=0.0298$. Mass discrimination averaged 1.25%/AMU over the course of the experiments (average measured atmospheric $^{40}Ar/^{36}Ar=281.5\pm0.75\%$).

Ages were calculated using the decay constants and isotopic abundances of Steiger and Jäger (1977). Uncertainties associated with the plateau and isochron ages are quoted at the 2$\sigma$ level and include both a 0.5% analytical uncertainty in the J factor and the uncertainty in the age of the flux monitor. The uncertainties for individual step ages reported in Table A6 represent only the analytical component of the total uncertainty.



Please cite this article as: Krebs, M., et al., The dynamics of intra-oceanic subduction zones: A direct comparison between fossil petrological evidence (Rio San Juan Complex, Dominican Republic) and numerical simulation, Lithos (2007), doi:10.1016/j.lithos.2007.09.003

Table A1
Electron microprobe analyses of minerals used for P–T determinations of the indicated P–T-path coordinates

**Garnet**

| Rock type | Eclogite | | |
|---|---|---|---|
| Sample | 25323/A(1) | 25323/B(1) | 25323/C(1) |
| $SiO_2$ | 37.02 | 37.68 | 36.70 |
| $TiO_2$ | 0.09 | 0.07 | 0.07 |
| $Al_2O_3$ | 21.04 | 21.38 | 21.41 |
| $Cr_2O_3$ | 0.12 | 0.06 | 0.07 |
| FeO | 19.69 | 21.85 | 22.22 |
| MnO | 6.24 | 2.54 | 2.75 |
| MgO | 1.28 | 3.34 | 1.58 |
| CaO | 14.18 | 13.50 | 14.37 |
| BaO | 0.11 | 0.00 | 0.00 |
| $Na_2O$ | 0.00 | 0.03 | 0.01 |
| $K_2O$ | 0.01 | 0.03 | 0.00 |
| Total | 99.78 | 100.48 | 99.18 |
| Si | 2.945 | 2.940 | 2.928 |
| $Al^{IV}$ | 0.055 | 0.060 | 0.072 |
| Σ | 3.000 | 3.000 | 3.000 |
| $Fe^{3+}$ | 0.070 | 0.087 | 0.051 |
| $Al^{VI}$ | 1.917 | 1.906 | 1.941 |
| Cr | 0.008 | 0.004 | 0.004 |
| Ti | 0.005 | 0.004 | 0.004 |
| Σ | 2.000 | 2.000 | 2.000 |
| Mg | 0.152 | 0.389 | 0.188 |
| Ca | 1.208 | 1.128 | 1.228 |
| Mn | 0.421 | 0.168 | 0.186 |
| $Fe^{2+}$ | 1.240 | 1.339 | 1.432 |
| Σ | 3.021 | 3.024 | 3.033 |
| Total | 13.021 | 13.024 | 13.033 |
| $X_{Mg}$ | 0.109 | 0.225 | 0.116 |
| Prp | 5.0 | 12.9 | 6.2 |
| Alm | 41.0 | 44.2 | 47.2 |
| Sps | 13.9 | 5.5 | 6.1 |
| Grs | 39.9 | 37.2 | 40.5 |

**K-white mica**

| Rock type | Eclogite | | | Omphacite blueschist | | Jadeite blueschist |
|---|---|---|---|---|---|---|
| Sample | 25323/B(1) | 25323/C(1) | 25323/D(1) | 25243/A(2) | 25243/B(2) | 25356/B(3) |
| $SiO_2$ | 48.77 | 49.14 | 50.00 | 49.01 | 50.85 | 53.40 |
| $TiO_2$ | 0.26 | 0.09 | 0.00 | 0.44 | 0.07 | 0.08 |
| $Al_2O_3$ | 27.02 | 23.52 | 26.95 | 29.62 | 24.42 | 24.07 |
| $Cr_2O_3$ | 0.04 | 0.01 | 0.62 | 0.00 | 0.00 | 0.00 |
| FeO | 3.07 | 5.85 | 3.10 | 2.35 | 3.88 | 1.37 |
| MnO | 0.07 | 0.08 | 0.33 | 0.03 | 0.02 | 0.04 |
| MgO | 3.15 | 3.79 | 3.12 | 2.86 | 3.39 | 5.14 |
| CaO | 0.08 | 0.88 | 0.01 | 0.00 | 0.06 | 0.00 |
| BaO | 0.92 | 0.72 | 1.91 | 0.43 | 0.64 | 0.18 |
| $Na_2O$ | 0.61 | 0.32 | 0.55 | 1.03 | 0.12 | 0.18 |
| $K_2O$ | 10.12 | 9.25 | 10.32 | 9.27 | 9.22 | 11.00 |
| F | 0.00 | 0.01 | 0.01 | 0.00 | 0.00 | 0.00 |
| Total | 94.11 | 93.64 | 96.91 | 95.04 | 92.67 | 95.48 |
| Si | 3.342 | 3.421 | 3.358 | 3.281 | 3.505 | 3.548 |
| $Al^{IV}$ | 0.658 | 0.579 | 0.642 | 0.719 | 0.495 | 0.452 |
| Σ | 4.000 | 4.000 | 4.000 | 4.000 | 4.000 | 4.000 |
| Ti | 0.013 | 0.005 | 0.000 | 0.022 | 0.004 | 0.004 |
| $Al^{VI}$ | 1.524 | 1.351 | 1.492 | 1.617 | 1.488 | 1.433 |
| Cr | 0.002 | 0.001 | 0.033 | 0.000 | 0.000 | 0.000 |
| Mg | 0.321 | 0.393 | 0.312 | 0.285 | 0.348 | 0.509 |
| Mn | 0.004 | 0.005 | 0.019 | 0.002 | 0.001 | 0.003 |
| $Fe^{2+}$ | 0.176 | 0.340 | 0.174 | 0.132 | 0.224 | 0.076 |
| Σ | 2.041 | 2.094 | 2.030 | 2.058 | 2.065 | 2.025 |
| Ca | 0.006 | 0.065 | 0.001 | 0.000 | 0.004 | 0.000 |
| Na | 0.082 | 0.043 | 0.065 | 0.134 | 0.016 | 0.023 |
| K | 0.885 | 0.821 | 0.884 | 0.792 | 0.811 | 0.932 |
| Ba | 0.025 | 0.020 | 0.050 | 0.011 | 0.017 | 0.005 |
| Σ | 0.997 | 0.949 | 1.000 | 0.937 | 0.848 | 0.960 |
| Total | 7.038 | 7.043 | 7.030 | 6.995 | 6.913 | 6.985 |
| $X_{Mg}$ | 0.646 | 0.536 | 0.642 | 0.684 | 0.608 | 0.870 |

**Chlorite**

| Rock type | Eclogite | Omphacite blueschist | | Jadeite blueschist |
|---|---|---|---|---|
| Sample | 25323/D(1) | 25243/B(2) | 25243/C(2) | 25356/B(3) |
| $SiO_2$ | 27.68 | 26.40 | 25.79 | 30.08 |
| $TiO_2$ | 0.03 | 0.04 | 0.04 | 0.01 |
| $Al_2O_3$ | 18.22 | 19.36 | 19.76 | 19.22 |
| $Cr_2O_3$ | 0.07 | 0.00 | 0.04 | 0.00 |
| FeO | 22.54 | 25.77 | 31.18 | 12.49 |
| MnO | 0.24 | 0.34 | 0.05 | 0.43 |
| MgO | 18.46 | 15.34 | 10.89 | 25.08 |
| CaO | 0.13 | 0.08 | 0.09 | 0.03 |
| BaO | 0.02 | 0.08 | 0.03 | 0.05 |
| $Na_2O$ | 0.00 | 0.02 | 0.19 | 0.01 |
| $K_2O$ | 0.01 | 0.00 | 0.07 | 0.03 |
| F | 0.00 | 0.00 | 0.01 | 0.00 |
| Total | 87.40 | 87.43 | 88.13 | 87.43 |
| Si | 2.884 | 2.802 | 2.792 | 2.957 |
| $Al^{IV}$ | 1.116 | 1.198 | 1.208 | 1.043 |
| Σ | 4.000 | 4.000 | 4.000 | 4.000 |
| Ti | 0.002 | 0.003 | 0.003 | 0.001 |
| $Al^{VI}$ | 1.121 | 1.223 | 1.314 | 1.185 |
| Cr | 0.006 | 0.000 | 0.003 | 0.000 |
| Mg | 2.866 | 2.427 | 1.758 | 3.675 |
| Mn | 0.021 | 0.031 | 0.005 | 0.036 |
| $Fe^{2+}$ | 1.964 | 2.287 | 2.823 | 1.027 |
| Ca | 0.015 | 0.009 | 0.010 | 0.003 |
| Ba | 0.001 | 0.003 | 0.001 | 0.002 |
| Na | 0.000 | 0.004 | 0.040 | 0.002 |
| K | 0.001 | 0.000 | 0.010 | 0.004 |
| Σ | 5.996 | 5.987 | 5.967 | 5.934 |
| Total | 9.996 | 9.987 | 9.967 | 9.934 |
| $X_{Mg}$ | 0.593 | 0.515 | 0.384 | 0.782 |

**Epidote**

| Rock type | Eclogite | Omphacite blueschist | | |
|---|---|---|---|---|
| Sample | 25323/B(1) | 25243/A(2) | 25243/B(2) | 25243/C(2) |
| $SiO_2$ | 37.90 | 38.21 | 38.19 | 37.85 |
| $TiO_2$ | 0.11 | 0.03 | 0.11 | 0.03 |
| $Al_2O_3$ | 24.43 | 25.48 | 26.26 | 23.20 |
| $Fe_2O_3$ | 11.89 | 11.06 | 10.18 | 13.81 |
| $Cr_2O_3$ | 0.10 | 0.11 | 0.12 | 0.18 |
| MnO | 0.20 | 0.12 | 0.04 | 0.25 |
| MgO | 0.08 | 0.07 | 0.05 | 0.02 |
| CaO | 23.18 | 23.34 | 23.55 | 23.25 |
| BaO | 0.33 | 0.01 | 0.06 | 0.02 |
| Na2O | 0.04 | 0.01 | 0.00 | 0.00 |
| Total | 98.26 | 98.43 | 98.56 | 98.61 |
| Si | 3.001 | 2.998 | 2.985 | 2.999 |
| $Al^{IV}$ | | 0.002 | 0.015 | 0.001 |
| Σ | 3.001 | 3.000 | 3.000 | 3.000 |
| Ti | 0.007 | 0.002 | 0.006 | 0.002 |
| $Al^{VI}$ | 2.281 | 2.355 | 2.404 | 2.166 |
| $Fe^{3+}$ | 0.708 | 0.653 | 0.599 | 0.823 |
| Cr | 0.006 | 0.007 | 0.007 | 0.011 |
| Σ | 3.002 | 3.016 | 3.016 | 3.002 |
| Mg | 0.009 | 0.008 | 0.006 | 0.002 |
| $Mn^{2+}$ | 0.013 | 0.008 | 0.003 | 0.017 |
| Ca | 1.967 | 1.962 | 1.972 | 1.976 |
| Ba | 0.005 | 0.001 | 0.002 | 0.001 |
| Na | 0.006 | 0.001 | 0.000 | 0.000 |
| Σ | 2.000 | 1.980 | 1.982 | 1.996 |
| Total | 8.003 | 7.996 | 7.998 | 7.998 |
| $X_{Fe^{3+}}$ | 0.236 | 0.217 | 0.199 | 0.274 |

(continued on next page)

Please cite this article as: Krebs, M., et al., The dynamics of intra-oceanic subduction zones: A direct comparison between fossil petrological evidence (Rio San Juan Complex, Dominican Republic) and numerical simulation, Lithos (2007), doi:10.1016/j.lithos.2007.09.003

Table A1 *continued*

**Amphibole**

| Rock type | Eclogite | | | | | Omphacite blueschist | | | | Jadeite blueschist |
|---|---|---|---|---|---|---|---|---|---|---|
| Sample | 25323/ Parg | 25323/ Mg-Tar | 25323/ Mg-Kat | 25323/ C(1) | 25323/ D(1) | 25243/ A(2) | 25243/ Win-A(2) | 25243/ B(2) | 25243/ C(2) | 25356/ B(3) |
| $SiO_2$ | 44.55 | 43.29 | 45.99 | 53.19 | 56.74 | 56.52 | 55.36 | 52.61 | 49.91 | 59.63 |
| $TiO_2$ | 0.45 | 0.57 | 0.31 | 0.10 | 0.01 | 0.07 | 0.02 | 0.24 | 0.16 | 0.00 |
| $Al_2O_3$ | 15.70 | 16.51 | 14.39 | 2.82 | 11.42 | 10.71 | 3.58 | 8.32 | 8.55 | 11.99 |
| $Cr_2O_3$ | 0.11 | 0.17 | 0.27 | 0.00 | 0.06 | 0.04 | 0.02 | 0.01 | 0.06 | 0.01 |
| FeO | 10.42 | 11.22 | 10.46 | 16.46 | 9.81 | 16.77 | 18.30 | 7.72 | 12.82 | 6.20 |
| MnO | 0.07 | 0.06 | 0.07 | 0.01 | 0.16 | 0.13 | 0.11 | 0.17 | 0.00 | 0.09 |
| MgO | 12.65 | 12.48 | 12.19 | 12.24 | 9.90 | 5.75 | 10.20 | 15.82 | 12.78 | 11.99 |
| CaO | 10.50 | 9.17 | 9.18 | 9.53 | 1.41 | 0.36 | 9.05 | 9.33 | 10.23 | 0.02 |
| BaO | 0.03 | 0.04 | 0.03 | 0.01 | 0.00 | 0.00 | 0.00 | 0.02 | 0.01 | 0.00 |
| $Na_2O$ | 3.49 | 4.61 | 4.15 | 1.95 | 6.71 | 7.14 | 2.15 | 2.66 | 2.59 | 7.68 |
| $K_2O$ | 0.47 | 0.52 | 0.40 | 0.15 | 0.06 | 0.01 | 0.12 | 0.20 | 0.10 | 0.01 |
| Total | 98.44 | 98.64 | 97.41 | 96.45 | 96.28 | 97.50 | 98.91 | 97.10 | 97.21 | 97.62 |
| Si | 6.356 | 6.160 | 6.615 | 7.804 | 7.901 | 7.992 | 7.978 | 7.371 | 7.215 | 7.999 |
| $Al^{IV}$ | 1.644 | 1.840 | 1.385 | 0.196 | 0.099 | 0.008 | 0.022 | 0.629 | 0.785 | 0.001 |
| Σ | 8.000 | 8.000 | 8.000 | 8.000 | 8.000 | 8.000 | 8.000 | 8.000 | 8.000 | 8.000 |
| $Al^{VI}$ | 0.997 | 0.930 | 1.055 | 0.291 | 1.776 | 1.777 | 0.586 | 0.745 | 0.672 | 1.895 |
| Ti | 0.048 | 0.061 | 0.034 | 0.011 | 0.001 | 0.007 | 0.002 | 0.025 | 0.017 | 0.000 |
| $Fe^{3+}$ | 0.276 | 0.606 | 0.171 | 0.304 | 0.071 | 0.143 | 0.013 | 0.273 | 0.158 | 0.099 |
| Cr | 0.012 | 0.019 | 0.031 | 0.000 | 0.007 | 0.004 | 0.002 | 0.001 | 0.007 | 0.001 |
| Mg | 2.691 | 2.647 | 2.614 | 2.677 | 2.055 | 1.212 | 2.191 | 3.304 | 2.754 | 2.398 |
| $Fe^{2+}$ | 0.967 | 0.730 | 1.087 | 1.715 | 1.072 | 1.841 | 2.193 | 0.632 | 1.392 | 0.597 |
| Mn | 0.008 | 0.007 | 0.009 | 0.001 | 0.019 | 0.016 | 0.013 | 0.020 | 0.000 | 0.010 |
| Σ | 4.999 | 5.000 | 5.001 | 4.999 | 5.001 | 5.000 | 5.000 | 5.000 | 5.000 | 5.000 |
| Ca | 1.605 | 1.398 | 1.415 | 1.498 | 0.210 | 0.055 | 1.397 | 1.401 | 1.585 | 0.003 |
| $Na^{M4}$ | 0.395 | 0.602 | 0.585 | 0.502 | 1.790 | 1.945 | 0.601 | 0.599 | 0.415 | 1.997 |
| Σ | 2.000 | 2.000 | 2.000 | 2.000 | 2.000 | 2.000 | 1.998 | 2.000 | 2.000 | 2.000 |
| $Na^{A}$ | 0.571 | 0.670 | 0.572 | 0.053 | 0.022 | 0.012 | 0.000 | 0.123 | 0.311 | 0.001 |
| K | 0.086 | 0.094 | 0.073 | 0.028 | 0.011 | 0.002 | 0.022 | 0.036 | 0.018 | 0.002 |
| Σ | 0.657 | 0.764 | 0.645 | 0.081 | 0.033 | 0.014 | 0.022 | 0.159 | 0.329 | 0.003 |
| Total | 15.656 | 15.765 | 15.646 | 15.081 | 15.033 | 15.014 | 15.020 | 15.159 | 15.329 | 15.002 |
| $X_{Mg}$ | 0.736 | 0.784 | 0.706 | 0.609 | 0.657 | 0.397 | 0.500 | 0.840 | 0.664 | 0.801 |

**Clinopyroxene**

| Rock type | Eclogite | | | | Omphacite blueschist | | Jadeite blueschist |
|---|---|---|---|---|---|---|---|
| Sample | 25323/ A(1) | 25323/ B(1) | 25323/ C(1) | 25323/ D(1) | 25243/ A(2) | 25243/ B(2) | 25356/B(3) |
| $SiO_2$ | 53.67 | 54.88 | 54.56 | 52.65 | 54.85 | 56.52 | 58.76 |
| $TiO_2$ | 0.11 | 0.08 | 0.12 | 0.12 | 0.27 | 0.03 | 0.62 |
| $Al_2O_3$ | 3.73 | 8.64 | 9.55 | 6.47 | 2.54 | 9.35 | 22.00 |
| $Cr_2O_3$ | 0.11 | 0.13 | 0.05 | 0.08 | 0.04 | 0.02 | 0.00 |
| FeO | 9.02 | 6.64 | 7.69 | 8.13 | 21.14 | 5.87 | 1.88 |
| MnO | 0.12 | 0.11 | 0.14 | 0.13 | 0.00 | 0.02 | 0.01 |
| MgO | 9.55 | 7.92 | 6.62 | 8.60 | 3.51 | 8.61 | 1.52 |
| CaO | 19.61 | 15.76 | 13.58 | 18.25 | 9.91 | 14.22 | 2.12 |
| BaO | 0.00 | 0.07 | 0.00 | 0.00 | 0.01 | 0.05 | 0.06 |
| $Na_2O$ | 3.68 | 5.83 | 6.85 | 5.13 | 7.92 | 5.99 | 13.78 |
| $K_2O$ | 0.02 | 0.00 | 0.00 | 0.03 | 0.00 | 0.03 | 0.02 |
| Total | 100.06 | 100.24 | 99.56 | 100.46 | 100.17 | 100.71 | 100.76 |
| Si | 1.983 | 1.980 | 1.980 | 1.920 | 2.001 | 2.002 | 1.992 |
| $Al^{IV}$ | 0.017 | 0.020 | 0.020 | 0.080 | 0.000 | 0.000 | 0.008 |
| Σ | 2.000 | 2.000 | 2.000 | 2.000 | 2.001 | 2.002 | 2.000 |
| $Al^{VI}$ | 0.146 | 0.348 | 0.389 | 0.198 | 0.154 | 0.407 | 0.870 |
| Ti | 0.003 | 0.002 | 0.003 | 0.003 | 0.008 | 0.001 | 0.016 |
| Cr | 0.003 | 0.004 | 0.002 | 0.002 | 0.001 | 0.001 | 0.000 |
| $Fe^{3+}$ | 0.127 | 0.072 | 0.105 | 0.237 | 0.353 | 0.001 | 0.013 |
| $Fe^{2+}$ | 0.152 | 0.129 | 0.128 | 0.011 | 0.316 | 0.175 | 0.040 |
| Mn | 0.004 | 0.003 | 0.004 | 0.004 | 0.000 | 0.001 | 0.000 |
| Mg | 0.526 | 0.426 | 0.358 | 0.467 | 0.196 | 0.457 | 0.077 |
| Σ | 0.960 | 0.983 | 0.990 | 0.923 | 1.027 | 1.042 | 1.017 |
| Ca | 0.776 | 0.609 | 0.528 | 0.713 | 0.397 | 0.543 | 0.077 |
| Na | 0.263 | 0.408 | 0.482 | 0.363 | 0.574 | 0.414 | 0.906 |
| K | 0.001 | 0.000 | 0.000 | 0.001 | 0.000 | 0.001 | 0.001 |
| Σ | 1.040 | 1.017 | 1.011 | 1.077 | 0.971 | 0.957 | 0.984 |
| Total | 4.000 | 4.000 | 4.000 | 4.000 | 4.000 | 4.000 | 4.000 |

**Plagio-clase**

| Rock type | Omp blueschist |
|---|---|
| Sample | 25243/C(2) |
| $SiO_2$ | 65.95 |
| $TiO_2$ | 0.01 |
| $Al_2O_3$ | 20.48 |
| $Cr_2O_3$ | 0.02 |
| FeO | 0.61 |
| MnO | 0.06 |
| MgO | 0.05 |
| CaO | 1.55 |
| BaO | 0.11 |
| $Na_2O$ | 9.92 |
| $K_2O$ | 1.08 |
| F | 0.01 |
| Total | 99.84 |
| Si | 2.917 |
| Al | 1.067 |
| $Fe^{3+}$ | 0.020 |
| Σ | 4.004 |
| Mg | 0.003 |
| Ca | 0.073 |
| Ba | 0.002 |
| Na | 0.851 |
| K | 0.061 |
| Σ | 0.990 |
| Total | 4.994 |
| An | 7.4 |
| Ab | 86.0 |
| Or | 6.2 |



Please cite this article as: Krebs, M., et al., The dynamics of intra-oceanic subduction zones: A direct comparison between fossil petrological evidence (Rio San Juan Complex, Dominican Republic) and numerical simulation, Lithos (2007), doi:10.1016/j.lithos.2007.09.003

Table A2
Activity models used for TWQ (TWQ), Thermocalc (TH) and/or PT pseudosection (Ps) calculations

| Mineral | Components | Description | Activity formulation |
|---|---|---|---|
| Aegirine–augite (Agt) TWQ, TH | Jadeite: $[Na]^{M2}[Al]^{M1}[Si]^{T_2}O_6$<br>Diopside: $[Ca]^{M2}[Mg]^{M1}[Si]^{T_2}O_6$<br>Hedenbergite: $[Ca]^{M2}[Fe^{2+}]^{M1}[Si]^{T_2}O_6$<br>Ca-Tschermak: $[Ca]^{M2}[Al]^{M1}[Al]^{T}[Si]^{T}O_6$<br>Acmite: $[Na]^{M2}[Fe^{3+}]^{M1}[Si]^{T_2}O_6$ | Assumed P2/n ordered pyroxene with ideal coupled mixing | Holland (2002) |
| Na-Amphibole (Nam) TWQ, TH | Glaucophane: $Na_2[Mg]_3^{M1,3}[Al]_2^{M2}$ $[Si]_4^{T1}Si_4O_{22}(OH)_2$<br>Ferro-glaucophane: $Na_2[Fe^{2+}]_3^{M1,3}$ $[Al]_2^{M2}[Si]_4^{T1}Si_4O_{22}(OH)_2$<br>Riebeckite: $Na_2[Fe^{2+}]_3^{M1,3}[Fe^{3+}]_2^{M2}[Si]_4^{T1}$ $Si_4O_{22}(OH)_2$ | Ideal mixing model with half $S_{mix}$ on $T_1$ | Holland (2002) |
| Ca– and Na–Ca-Amphibole (Amp) TWQ, TH | Pargasite: $[Na]^{A}[Ca]_2^{M4}[Mg]_3^{M1,3}[Al]_2^{M2}$ $[Al]_2^{T1}[Si]_2^{T1}$ $Si_4O_{22}(OH)_2$<br>Glaucophane: $[0]^{A}[Na]_2^{M4}[Mg]_3^{M1,3}[Al]_2^{M2}$ $[Si]_4^{T1}Si_4O_{22}(OH)_2$<br>Tschermakite: $[0]^{A}[Ca]_2^{M4}[Mg]_3^{M1,3}[Al]_2^{M2}$ $[Al]_2^{T1}[Si]_2^{T1}Si_4O_{22}(OH)_2$<br>Tremolite: $[0]^{A}[Ca]_2^{M4}[Mg]_3^{M1,3}[Mg]_2^{M2}$ $[Si]_4^{T1}Si_4O_{22}(OH)_2$<br>Ferroactinolite: $[0]^{A}[Ca]_2^{M4}[Fe]_3^{M1,3}[Fe]_2^{M2}$ $[Si]_4^{T1}Si_4O_{22}(OH)_2$ | Non-ideal mixing model with half Smix 2 on $T_1$ | Holland and Blundy (1994) |
| Ca– and Na–Ca –Amphibole (Amp) for *T*>550 °C TWQ, TH | Pargasite: $[Na]^{A}[Ca]_2^{M4}[Mg]_3^{M1,3}[Al]_2^{M2}$ $[Al]_2^{T1}[Si]_2^{T1}Si_4O_{22}(OH)_2$<br>Glaucophane: $[0]^{A}[Na]_2^{M4}[Mg]_3^{M1,3}$ $[Al]_2^{M2}[Si]_4^{T1}Si_4O_{22}(OH)_2$<br>Tschermakite: $[0]^{A}[Ca]_2^{M4}[Mg]_3^{M1,3}$ $[Al]_2^{M2}[Al]_2^{T1}[Si]_2^{T1}Si_4O_{22}(OH)_2$<br>Tremolite: $[0]^{A}[Ca]_2^{M4}[Mg]_3^{M1,3}$ $[Mg]_2^{M2}[Si]_4^{T1}Si_4O_{22}(OH)_2$<br>Ferroactinolite: $[0]^{A}[Ca]_2^{M4}$ $[Fe]_3^{M1,3}[Fe]_2^{M2}[Si]_4^{T1}Si_4O_{22}(OH)_2$ | Non-ideal mixing model | Dale et al. (2000) |
| Phengite (Phe) TWQ | Muscovite: $[K]^{A}[Al]^{M2}[Al]^{M2}[Si]^{T2}$ $[Al]^{T2}Si_2O_{10}(OH)_2$<br>Mg–Al–celadonite: $[K]^{A}[Mg]^{M1}[Al]^{M2}$ $[Mg]^{M2}[Si]^{T2}[Al]^{T2}$ $Si_2O_{10}(OH)_2$<br>Fe–Al–celadonite: $[K]^{A}[Fe]^{M1}[Al]^{M2}$ $[Fe]^{M2}[Si]^{T2}[Al]^{T2}$ $Si_2O_{10}(OH)_2$<br>Paragonite: $[Na]^{A}[Al]^{M2}[Al]^{M2}[Si]^{T2}$ $[Al]^{T2}$ $Si_2O_{10}(OH)_2$ | | Parra et al. (2002) |
| Chlorite (Chl) TWQ | Clinochlore: $[Mg]^{A4}{}_4[Mg]^{M2}[Al]^{M2}$ $[Si]^{T2}[Al]^{T2}Si_2O_{10}(OH)_8$<br>Daphnite: $[Fe]^{A4}{}_4[Fe]^{M2}[Al]^{M2}[Si]^{T2}$ $[Al]^{T2}Si_2O_{10}(OH)_8$<br>Amesite: $[Mg]^{A4}{}_4[Al]^{M2}2[Al]^{T2}{}_2Si_2O_{10}(OH)_8$ | | Vidal et al. (2001) |
| Clino-pyroxene (Cpx) TWQ, TH, Ps | Jadeite: $[Na]^{M2}[Al]^{M1}Si_2O_6$<br>Diopside: $[Ca]^{M2}[Mg]^{M1}Si_2O_6$<br>Hedenbergite: $[Ca]^{M2}[Fe^{2+}]^{M1}Si_2O_6$ | Polynominal fit to the results of a CVM model | Vinograd (2002a,b) |
| Garnet (Grt) TWQ, TH, Ps | Pyrope: $[Mg]^{A}{}_3Al_2Si_3O_8$<br>Almandine: $[Fe^{2+}]^{A}{}_3Al_2Si_3O_8$<br>Grossular: $[Ca]^{A}{}_3Al_2Si_3O_8$ | Mixing on site, regular solution gammas | Dale et al. (2000) |
| Phengite (Phe) TH, Ps | Muscovite: $[K]^{A}[Al]^{M2a}[Al]^{M2b}$ $[Al]^{T1}[Si]^{T1}Si_2$ $O_{10}(OH)_2$<br>Mg–Al–celadonite: $[K]^{A}[Mg]^{M2a}[Al]^{M2b}$ $[Si]^{T1}{}_2Si_2$ $O_{10}(OH)_2$<br>Fe–Al–celadonite: $[K]^{A}[Fe^{2+}]^{M2a}[Al]^{M2b}$ $[Si]^{T1}{}_2Si_2O_{10}(OH)_2$ | Mixing on sites, non ideal contributions given by the van Laar model expressions | Coggon and Holland (2002) |

(continued on next page)



Please cite this article as: Krebs, M., et al., The dynamics of intra-oceanic subduction zones: A direct comparison between fossil petrological evidence (Rio San Juan Complex, Dominican Republic) and numerical simulation, Lithos (2007), doi:10.1016/j.lithos.2007.09.003

Table A2 (*continued*)

| Mineral | Components | Description | Activity formulation |
|---|---|---|---|
| | Paragonite: $[Na]^{A}[Al]^{M2a}[Al]^{M2b}[Al]^{T1}[Si]^{T1}Si_2O_{10}(OH)_2$ | | |
| Paragonite (Pa) TH, Ps | Paragonite: $[Na]^{A}Al_3Si_3O_{10}(OH)_2$<br>Margarite: $[Ca]^{A}Al_4Si2O10(OH)_2$ | DQF model for Na–Ca mixing | (Vance and Holland, 1993; Will et al., 1998) |
| Biotite (Bt) TH, Ps | Phlogopite: $K[Mg]^{M1}[Mg]^{M2}{}_2[Al]^{T1}[Si]^{T1}Si_2O_{10}(OH)_2$<br>Annite: $K[Fe]^{M1}[Fe]^{M2}{}_2[Al]^{T1}[Si]^{T1}Si_2O_{10}(OH)_2$<br>Eastonite: $K[Al]^{M1}[Mg]^{M2}{}_2[Al]^{T1}{}_2Si_2O_{10}(OH)_2$<br>Ordered biotite: $K[Fe]^{M1}[Mg]^{M2}{}_2[Al]^{T1}[Si]^{T1}Si_2O_{10}(OH)_2$ | Order-disorder of Mg and $Fe^{2+}$ between "$M_1$ site" and "$M_2$ sites", $Al^{M1}$ odered, regular solution gammas | Powell and Holland (1999) |
| Chlorite (Chl) TH, Ps | Clinochlore: $[Mg]^{M2,3}{}_4[Mg]^{M1}[Al]^{M4}[Al]^{T2}[Si]^{T2}Si_2O_{10}(OH)_8$<br>Daphnite: $[Fe^{2+}]^{M2,3}{}_4[Fe^{2+}]^{M1}[Al]^{M4}[Al]^{T2}[Si]^{T2}Si_2O_{10}(OH)_8$<br>Amesite: $[Mg]^{M2,3}{}_4[Al]^{M1}[Al]^{M4}[Al]^{T2}{}_2Si_2O_{10}(OH)_8$<br>Al-free chlorite: $[Mg]^{M2,3}{}_4[Mg]^{M1}[Mg]^{M4}[Si]^{T2}{}_2Si_2O_{10}(OH)_8$ | Ordering of octahedral Al into the "$M_4$ site", regular solution gammas | Holland et al. (1998b) Q5 |
| Epidote (Ep) TWQ, TH, Ps | Clinozoisite: $Ca_2Al[Al]^{M1}[Al]^{M3}$<br>Fe-epidote: $Ca_2Al\ [Fe^{3+}]^{M1}[Fe^{3+}]^{M3}$<br>Epidote: $Ca_2Al\ [Al]^{M1}[Fe^{3+}]^{M3}$ | Order-disorder of Al and $Fe^{3+}$ between "$M_1$ and $M_3$ site", regular solution gammas | Holland (1999) |
| Plagioclase (Pl) TWQ, TH, Ps | Anorthite: $[Ca]^{A}Al_2Si_2O_8$<br>Albite: $[Na]^{A}AlSi_3O_8$ | DQF and regular solution model with regular solution gammas for Na–Ca mixing | Holland and Powell (1992, 1996a,b) |

Table A3
Rb-Sr isotopic data for eclogite 25323, omphacite blueschist 25243 and jadeite blueschist 25356

| Sample | Grain-size [μm] | $^{87}Rb/^{86}Sr$ | $^{87}Sr/^{86}Sr$ | Initial $^{87}Sr/^{86}Sr$ | Calculated ages [Ma] |
|---|---|---|---|---|---|
| Eclogite 25323 | | | | 0.704659±0.000011 | 74.7±0.5 |
| WR | Powder | 0.396 | 0.705079±0.000010 | | |
| Garnet | 250–355 | 17.547 | 0.723253±0.000023 | | |
| Phengite fine | 125–180 | 58.524 | 0.7664126±0.000028 | | |
| Phengite coarse | 250–355 | 52.809 | 0.760826±0.000030 | | |
| Omphacite blueschist 25243 | | | | 0.704758±0.000011 | 80.3±1.1 |
| WR | Powder | 0.216 | 0.705005±0.000009 | | |
| Amphibole | 180–250 | 0.739 | 0.705601±0.000010 | | |
| Phengite | 250–355 | 4.855 | 0.710295±0.000044 | | |
| Jadeite blueschist 25356 | | | | 0.706278±0.000017 | 62.1±1.4 |
| WR | Powder | 1.297 | 0.707404±0.000010 | | |
| Glaucophane | 180–250 | 0.586 | 0.706843±0.000025 | | |
| Phengite | 180–250 | 16.384 | 0.720797±0.000015 | | |

Table A4
Lu-Hf isotopic data for eclogite 25323

| Sample | Grain-size [μm] | $^{176}Lu/^{177}Hf$ | $^{176}Hf/^{177}Hf$ | $\pm^{176}Hf/^{177}Hf$ | Initial $^{176}Hf/^{177}Hf$ | Calculated age [Ma] |
|---|---|---|---|---|---|---|
| Eclogite 25323 | | | | | 0.283072±0.000015 | 103.6±2.7 |
| Omphacite | 180–250 | 0.008 | 0.283079 | ±0.000023 | | |
| Epidote | 180–250 | 0.083 | 0.283238 | ±0.000020 | | |
| Amphibole | 180–250 | 0.004 | 0.283097 | ±0.000016 | | |
| Whole rock | Powder | 0.037 | 0.283133 | ±0.000014 | | |
| Garnet | 250–355 | 0.881 | 0.284789 | ±0.000032 | | |
| Garnet (1) | 180–250 | 0.367 | 0.283773 | ±0.000016 | | |
| Garnet | 180–250 | 0.465 | 0.283972 | ±0.000027 | | |

(1) fraction of inclusion-rich garnet.

Please cite this article as: Krebs, M., et al., The dynamics of intra-oceanic subduction zones: A direct comparison between fossil petrological evidence (Rio San Juan Complex, Dominican Republic) and numerical simulation, Lithos (2007), doi:10.1016/j.lithos.2007.09.003

Table A5
U–Pb isotopic data for eclogite 25323

| Sample | Concentrations | | | Measured isotope ratios | | |
|---|---|---|---|---|---|---|
| Eclogite 25323 | U [ppm] | Pb [ppm] | $^{206}Pb/^{204}Pb$ | $^{208}Pb/^{206}Pb$ | $^{207}Pb/^{206}Pb$ | ±2σ |
| 4064 | 1274 | 74 | 57.72 | 0.2232 | 0.05017 | 0.00184 |
| 4070 | 868 | 73 | 42.04 | 0.2376 | 0.05291 | 0.00306 |

| Sample | Corrected isotope ratios | | | | Apparent age (Ma) | | | RHO |
|---|---|---|---|---|---|---|---|---|
| Eclogite 25323 | $^{207}Pb/^{235}U$ | ±2σ | $^{206}Pb/^{238}U$ | ±2σ | $^{206}Pb/^{238}U$ | $^{207}Pb/^{235}U$ [Ma] | $^{207}Pb/^{206}Pb$ [Ma] | |
| 4064 | 0.1492 | 0.0062 | 0.02156 | 0.00019 | 137.5 | 141.2 | 203.0 | 0.63 |
| 4070 | 0.1589 | 0.0105 | 0.02179 | 0.00034 | 139.0 | 145.8 | 224.8 | 0.52 |

Table A6
$^{40}Ar/^{39}Ar$ release data for phengite from eclogite 25323 and omphacite blueschist 25243

| Temp [°C] | $^{40}Ar/^{39}Ar$ | $^{38}Ar/^{39}Ar$ | $^{37}Ar/^{39}Ar$ | $^{36}Ar/^{39}Ar$ | % $^{40}Ar^*$ | K/Ca | $^{40}Ar^*/^{39}Ar_K$ | Age [Ma] | Error [±2σ] |
|---|---|---|---|---|---|---|---|---|---|
| *Eclogite 25323* | | | | | | | | | |
| 600 | 1766.9 | 1.116 | 0.6038 | 5.658 | 5.28 | 0.7630 | 90.847 | 189.0 | 53.7 |
| 700 | 38.851 | 0.01496 | 0.02027 | 0.01204 | 90.76 | 21.21 | 35.263 | 75.71 | 1.92 |
| 770 | 37.008 | 0.01356 | 0.01203 | 0.00698 | 94.35 | 35.72 | 34.916 | 74.98 | 0.99 |
| 830 | 36.316 | 0.01357 | 0.00986 | 0.00614 | 94.92 | 43.61 | 34.472 | 74.05 | 0.57 |
| 870 | 36.062 | 0.01359 | 0.00157 | 0.00624 | 94.80 | 274.4 | 34.188 | 73.45 | 0.38 |
| 900 | 35.357 | 0.01248 | 0.00103 | 0.00368 | 95.91 | 656.5 | 34.231 | 73.54 | 0.38 |
| 920 | 35.351 | 0.01275 | −0.00061 | 0.00387 | 96.68 | 0.000 | 34.178 | 73.43 | 0.35 |
| 940 | 35.379 | 0.01307 | 0.00302 | 0.00391 | 96.65 | 142.2 | 34.194 | 73.47 | 0.38 |
| 960 | 35.209 | 0.01266 | 0.00091 | 0.00355 | 96.93 | 474.5 | 34.130 | 73.33 | 0.40 |
| 990 | 35.083 | 0.01294 | 0.00928 | 0.00325 | 97.18 | 46.31 | 34.094 | 73.26 | 0.39 |
| 1030 | 35.131 | 0.01266 | 0.01359 | 0.00236 | 97.93 | 31.62 | 34.405 | 73.91 | 0.40 |
| 1090 | 35.327 | 0.01216 | 0.04601 | 0.00204 | 98.21 | 9.341 | 34.697 | 74.52 | 0.85 |
| 1160 | 35.138 | 0.01311 | 0.5986 | 0.00185 | 98.49 | 0.7176 | 34.621 | 74.37 | 1.76 |
| 1350 | 34.607 | 0.01211 | 0.3513 | 0.00141 | 98.78 | 1.223 | 34.194 | 73.47 | 1.03 |
| | | | | | | | Plateau age | 73.42 | 0.74 |
| | | | | | | | Isochron age | 73.18 | 0.99 |
| *Omphacite blueschist 25243* | | | | | | | | | |
| 600 | 2226.4 | 1.404 | −0.5864 | 7.284 | 3.22 | 0.000 | 72.382 | 152.2 | 70.9 |
| 650 | 50.456 | 0.02056 | 0.1174 | 0.04450 | 73.60 | 3.663 | 37.137 | 79.69 | 2.49 |
| 700 | 44.101 | 0.01780 | 0.03208 | 0.02753 | 81.47 | 13.40 | 35.932 | 77.16 | 1.23 |
| 750 | 41.941 | 0.01603 | 0.00276 | 0.02270 | 83.92 | 155.5 | 35.199 | 75.62 | 0.76 |
| 790 | 43.942 | 0.01851 | 0.00258 | 0.02982 | 79.86 | 166.9 | 35.092 | 75.39 | 0.69 |
| 830 | 43.468 | 0.01737 | 0.00261 | 0.03016 | 79.41 | 164.8 | 34.517 | 74.18 | 0.50 |
| 870 | 41.411 | 0.01683 | 0.00096 | 0.02294 | 83.54 | 445.5 | 34.596 | 74.35 | 0.42 |
| 910 | 38.450 | 0.01533 | 0.00884 | 0.01369 | 87.67 | 46.21 | 34.376 | 73.88 | 0.44 |
| 950 | 37.197 | 0.01395 | −0.00075 | 0.01021 | 89.48 | 0.000 | 34.150 | 73.41 | 0.37 |
| 1000 | 39.434 | 0.01579 | 0.01212 | 0.01667 | 87.43 | 35.46 | 34.476 | 74.10 | 0.40 |
| 1050 | 37.093 | 0.01429 | 0.01543 | 0.00963 | 89.95 | 26.92 | 34.220 | 73.56 | 0.34 |
| 1100 | 36.679 | 0.01356 | 0.01832 | 0.00712 | 94.18 | 23.47 | 34.545 | 74.24 | 0.35 |
| 1170 | 38.528 | 0.01465 | 0.04563 | 0.01315 | 89.83 | 9.419 | 34.613 | 74.38 | 0.52 |
| 1350 | 49.868 | 0.02175 | 0.1491 | 0.05016 | 70.22 | 2.882 | 35.018 | 75.24 | 0.71 |
| | | | | | | | Plateau age | 73.85 | 0.79 |
| | | | | | | | Isochron age | 72.97 | 1.01 |



Please cite this article as: Krebs, M., et al., The dynamics of intra-oceanic subduction zones: A direct comparison between fossil petrological evidence (Rio San Juan Complex, Dominican Republic) and numerical simulation, Lithos (2007), doi:10.1016/j.lithos.2007.09.003

## References


Abbott, R.N., Draper, G., Keshav, 2005a. UHP magma paragenesis, garnet peridotite, and garnet pyroxenite: an example from the Dominican Republic. Int. Geol. Rev. 47, 233–247.

Abbott, R.N., Draper, G., Keshav, S., 2005b. UHP metamorphism in garnet peridotite, Cuaba unit, Rio San Juan Complex, Dominican Republic. In: Draper, G., Mitchell, S. (Eds.), Transactions of the 16th Caribbean Geological Conference, Barbados 16$^{th}$-21st July 2002. Caribb. J. Earth Sci., vol. 39, pp. 13–20 (Jamaica).

Amato, J.M., Johnson, L.P., Baumgartner, L.P., Beard, B.L., 1999. Rapid exhumation of the Zermatt-Saas ophiolite deduced from high-precision Sm–Nd and Rb–Sr geochronology. Earth Planet. Sci. Lett. 171, 425–438.

Anam, K., 1994. Petrology and geochemistry of some high pressure rocks from the northern part of the Rio San Juan Complex, Dominican Republic. Unpublished M.S. Thesis, Florida International University, Miami, Florida USA, 127 pp.

Berman, R.G., 1988. Internally-consistent thermodynamic data for minerals in the system $Na_2O–K_2O–CaO–MgO–FeO–Fe_2O_3–Al_2O_3–SiO_2–TiO_2–H_2O–CO_2$. J. Petrol. 29, 445–522.

Blake Jr., M.C., Moore, D.E., Jayko, A.S., 1995. The role of serpentinite melanges in the unroofing of UHPM rocks: An example from the Western Alps of Italy. In: Coleman, R.G., Wang, X. (Eds.), Ultrahigh Pressure Metamorphism. Cambridge University Press, New York, pp. 182–205.

Burke, K., 1988. Tectonic evolution of the Caribbean. Annu. Rev. Earth Planet. Sci. 16, 201–230.

Burke, K., Fox, P.J., Sengör, A.M.C., 1978. Buoyant ocean floor and the evolution of the Caribbean. J. Geophys. Res. B 83, 3949–3954.

Burke, K., Cooper, C., Dewey, J.F., Mann, P., Pindell, J.L., 1984. Caribbean tectonics and relative plate motions. In: Bonini, W.E., Hargraves, R.B., Shagam, R. (Eds.), The Caribbean South America Plate Boundary and Regional Tectonics. Geol. Soc. Amer. Mem., vol. 162, pp. 31–64.

Carson, C.J., Powell, R., Clarke, G.L., 1999. Calculated mineral equilibria for eclogites in $CaO–Na_2O–FeO–MgO–Al_2O_3–SiO_2–H_2O$: application to the Pouébo Terrane, Pam Peninsula, New Caledonia. J. Metamorph. Geol. 17, 9–24.

Carson, C.J., Clarke, G.L., Powell, R., 2000. Hydration of eclogite, Pam Peninsula, New Caledonia. J. Metamorph. Geol. 18, 79–90.

Carswell, D.A., O'Brien, P.J., Wilson, R.N., Zhai, M., 1997. Thermobarometry of phengite-bearing eclogites in the Dabie Mountains of central China. J. Metamorph. Geol. 15, 239–252.

Cloos, M., 1982. Flow melanges: Numerical modelling and geologic constraints on their origin in the Franciscan subduction complex, California. Geol. Soc. Amer. Bull. 93, 330–345.

Cloos, M., Shreve, R.L., 1988a. Subduction-channel model of prism accretion, melange formation, sediment subduction, and subduction erosion at convergent plate margins, 1, Background and description. Pure Appl. Geophys. 128, 455–00. Q7

Cloos, M., Shreve, R.L., 1988b. Subduction-channel model of prism accretion, melange formation, sediment subduction, and subduction erosion at convergent plate margins, 2, Implications and discussion. Pure Appl. Geophys. 128, 501–545.

Coggon, R., Holland, T.J.B., 2002. Mixing properties of phengitic micas and revised garnet-phengite thermobarometers. J. Metamorph. Geol. 20, 683–696.

Cosca, M.A., Sutter, J.F., Essene, E.J., 1991. Cooling and inferred uplift/erosion history of the Grenville Orogen, Ontario: Constraints from 40Ar/39Ar thermochronology. Tectonics 10, 959–977.

Dachs, E.A., Proyer, A., 2002. Constraints on the duration of high-pressure metamorphism in the Tauern Window from diffusion modeling of discontinuous growth zones in eclogite garnet. J. Metamorph. Geol. 20, 769–780.

Dale, J., Holland, T.J.B., Powell, R., 2000. Hornblende-garnet-plagioclase thermobarometry: a natural assemblage calibration of the thermodynamics of hornblende. Contrib. Mineral. Petrol. 140, 353–362.

Draper, G., Nagle, F., 1991. Geology, structure and tectonic development of the Rio San Juan Complex, northern Dominican Republic. Spec. Pap. - Geol. Soc. Am. 262, 77–95.

Draper, G., Guitierrez, G., Lewis, J.F., 1996. Thrust emplacement of the Hispaniola peridotite belt: orogenic expression of the mid Cretaceous Caribbean arc polarity reversal? Geology 24, 1143–1146.

Duchene, S., Blichert-Toft, J., Luais, B., Telouk, P., Lardaux, J.M., Albarede, F., 1997. The Lu–Hf dating of garnets and the ages of the Alpine high-pressure metamorphism. Nature 387, 586–589.

Ellis, D.J., Green, D.H., 1979. An experimental study of the effect of Ca upon garnet–clinopyroxene Fe-Mg exchange equilibria. Contrib. Mineral. Petrol. 71, 13–22.

Ernst, W.G., 1988. Tectonic history of subduction zones inferred from retrograde blueschist P–T paths. Geology 16, 1081–1084.

Evans, B.W., 1990. Phase relations of epidote-blueschists. Lithos 25, 3–23.

Fryer, P., Wheat, C.G., Mottl, M., 1999. Mariana blueschist mud volcanism: implications for conditions within the subduction zone. Geology 27, 103–106.

Ganguly, J., Tirone, M., Hervig, R.L., 1988. Diffusion kinetics of samarium and neodymium in garnet, and a method for determining cooling rates of rocks. Science 281, 805–807.

Gebauer, D., Schertl, H.-P., Brix, M., Schreyer, W., 1997. 35 Ma old ultrahigh-pressure metamorphism and evidence for very rapid exhumation in the Dora Maira Massif, Western Alps. Lithos 41, 5–24.

Gerya, T.V., Stöckhert, B., 2002. Exhumation rates of high pressure metamorphic rocks in subduction channels: the effect of rheology. Geophys. Res. Lett. 29, 1261. doi:10.1029/2001GL014307 102-1/4.

Gerya, T.V., Yuen, D.A., 2003a. Rayleigh-Taylor instabilities from hydration and melting propel "cold plumes" at subduction zones. Earth Planet. Sci. Lett. 212, 47–62.

Gerya, T.V., Yuen, D.A., 2003b. Characteristics-based marker-in-cell method with conservative finite-differences schemes for modeling geological flows with strongly variable transport properties. Phys. Earth Planet. Inter. 140, 295–320.

Gerya, T., Stöckhert, B., 2005. Two-dimensional numerical modeling of tectonic and metamorphic histories at active continental margins. Int. J. Earth. Sci. 94, 531–557.

Gerya, T.V., Perchuk, L.L., van Reenen, D.D., Smit, C.A., 2000. Two-dimensional numerical modeling of pressure–temperature-time paths for the exhumation of some granulite facies terrains in the Precambrian. J. Geodyn. 30, 17–35.

Gerya, T.V., Maresch, W.V., Willner, A.P., Van Reenen, D.D., Smit, C.A., 2001. Inherent gravitational instability of thickened continental crust with regionally developed low to medium-pressure granulite facies metamorphism. Earth Planet. Sci. Lett. 190, 221–235.

Gerya, T.V., Stöckhert, B., Perchuk, A.L., 2002. Exhumation of high-pressure metamorphic rocks in a subduction channel: a numerical simulation. Tectonics 142, 6–1-6-19.

Gerya, T.V., Yuen, D.A., Sevre, E.O.D., 2004. Dynamical causes for incipient magma chambers above slabs. Geology 32, 89–92.

Guillot, S., Hattori, K.H., de Sigoyer, J., 2000. Mantle wedge serpentinization and exhumation of eclogites: Insight from eastern Ladakh, northwest Himalaya. Geology 28, 199–202.




Please cite this article as: Krebs, M., et al., The dynamics of intra-oceanic subduction zones: A direct comparison between fossil petrological evidence (Rio San Juan Complex, Dominican Republic) and numerical simulation, Lithos (2007), doi:10.1016/j.lithos.2007.09.003

Guillot, S., Hattori, K.H., de Sigoyer, J., Nägler, T., Auzende, A.L., 2001. Evidence of hydration of the mantle wedge and its role in the exhumation of eclogites. Earth Planet. Sci. Lett. 193, 115–127.

Hames, W.E., Bowring, S.A., 1994. An empirical evaluation of the argon diffusion geometry in muscovite. Earth Planet. Sci. Lett. 124, 161–167.

Harlow, G.E., 1994. Jadeitites, albitites, and related rocks from the Motagua fault zone, Guatemala. J. Metamorph. Geol. 12, 49–68.

Harlow, G.E., Sisson, V.B., Ave Lallemant, H.G., Sorenson, S.S., 2003. High pressure metasomatic rocks along the Motagua Fault Zone, Guatemala. Ofioliti 28, 115–120.

Hawkesworth, C.J., van Calsteren, P., 1992. Geological time. In: Brown, G.C., Hawkesworth, C.J., Wilson, R.C.L. (Eds.), Understanding the Earth (a new Synthesis). Cambridge University Press. 551 pp.

Hermann, J., Muntener, O., Scambelluri, M., 2000. The importance of serpentinite mylonites for subduction and exhumation of oceanic crust. Tectonophysics 327, 225–238.

Holland, T.J.B., 1979. Reversed hydrothermal deterimination of jadeite-diopside activities. EOS. Trans. Am. Geophys. Union 60, 405.

Holland, T.J.B., 1980. The reaction albite = jadeite + quarz determined experimentally in the range 600–1200 °C. Am. Mineral. 65, 129–134.

Holland, T.J.B., 1983. The experimental determination of activities in disordered and short range ordered jadeitic pyroxenes. Contrib. Mineral. Petrol. 82, 214–220.

Holland, T.J.B., 1999. Epidotes. http://www.esc.cam.ac.uk/astaff/holland/ds5/epidotes/ep.html.

Holland, T.J.B., 2002. AX: A program to calculate activities of mineral endmembers from chemical analyses. http://www.esc.cam.ac.uk/astaff/holland/ax.html2002.

Holland, T.J.B., Powell, R., 1992. Plagioclase feldspars: activity-composition relations based on Darken's Quadratic Formalism and Landau theory. Am. Mineral. 77, 53–61.

Holland, T.J.B., Blundy, J.D., 1994. Non-ideal interactions in calcic amphiboles and their bearing on amphibole plagioclase thermometry. Contrib. Mineral. Petrol. 116, 433–447.

Holland, T., Powell, R., 1996a. Thermodynamics of order-disorder in minerals: I. Symmetric formalism applied to minerals of fixed composition. Am. Mineral. 81, 1413–1424.

Holland, T., Powell, R., 1996b. Thermodynamics of order-disorder in minerals: II. Symmetric formalism applied to solid solutions. Am. Mineral. 81, 1425–1437.

Holland, T.J.B., Powell, R., 1998a. An internally-consistent thermodynamic data set for phases of petrological interest. J. Metamorph. Geol. 16, 309–343.

Holland, T.J.B., Powell, R., 1998b. Mixing properties and activity-composition relationships of chlorites in the system MgO–FeO–$Al_2O_3$–$SiO_2$–$H_2O$. Eur. J. Mineral. 10, 395–406.

Holland, T.J.B., Powell, R., 2001. http://www.esc.cam.ac.uk/astaff/holland/thermocalc.html.

Hsu, K.J., 1971. Franciscan melange as a model for eugeosunclinal sedimentation and underthrusting tectonics. J. Geophys. Res. 76, 1162–1170.

Krebs, M., 2006, Geothermobarometrie und Geochronologie subduktionsbezogener Hochdruckmetamorphite des Rio San Juan Komplexes (nördliche Dominikanische Republik). unpubl. PhD Thesis, Ruhr-Universität Bochum, Bochum.

Krogh, T.E., 1973. A low contamination method for hydrothermal decomposition of zircon and extraction of U and Pb for isotopic age determinations. Geochim. Cosmochim. Acta 37, 485–494.

Krogh, T.E., 1982. Improved accuracy of U–Pb zircon ages by the creation of more concordant systems using an air abrasion technique. Geochim. Cosmochim. Acta 46, 637–649.

Krogh, E.J., 1988. The garnet–clinopyroxene Fe–Mg geothermometer-a reinterpretation of existing experimental data. Contrib. Mineral. Petrol. 99, 44–48.

Krogh, E.G., Oh, C.W., Liou, J.G., 1994. Polyphase and anticlockwise P–T evolution for the Franciscan eclogites and blueschists from Jenner, California, USA. J. Metamorph. Geol. 12, 121–134.

Lange, U., Bröcker, M., Mezger, K., Don, J., 2002. Geochemistry and Rb–Sr geochronology of a ductile shear zone in the Orlica–Snieznik dome (West Sudetes, Poland). Int. J. Earth Sci. 91, 1005–10016.

Lewis, J.F., Draper, G., Proenza, J., Espaillat, Jimenez, J., 2006. Ophiolite related ultramafic rocks (serpentinites) in the Caribbean region: a review of their occurrence, composition, origin, emplacement and Ni-laterite soil formation. Geologica Acta (Barcelona) 4 (1-2), 7–28.

Ludwig, K.R., 1991. ISOPLOT; a plotting and regression program for radiogenic-isotope data; version 2.53. U.S. Geol. Surv. Open-File Rep. 91–0445.

Ludwig, K.R., 2001. Isoplot/Ex version 2.49, A Geochronological Toolkit for Microsoft Excel, Berkeley Geochronology Center Special Publication 1a Nov. 20.

Maresch, W.V., Gerya, T.V., 2005. Blueschists and blue amphiboles: how much subduction do they need? Int. Geol. Rev. 47, 688–702.

Massonne, H-J., Szpurka, Z., 1997. Thermodynamic properties of white micas on the basis of high-pressure experiments in the systems $K_2O$–MgO–$Al_2O_3$–$SiO_2$–$H_2O$ and $K_2O$–FeO–$Al_2O_3$–$SiO_2$–$H_2O$. Lithos 41, 229–250.

McDougall, I., Roksandic, Z., 1974. Total fusion $^{40}Ar/^{39}Ar$ ages using HIFAR reactor. J. Geol. Soc. Aust. 21, 81–89.

Mezger, K., Hanson, G.N., Bohlen, S.R., 1989. High-precision U–Pb ages of metamorphic rutile: application to the cooling history of high-grade terranes. Earth Planet. Sci. Lett. 96, 106–118.

Münker, C., Weyer, S., Scherer, E., Mezger, K., 2001. Separation of high field strength elements (Nb, Ta, Zr, Hf) and Lu from rock samples for MC-ICPMS measurements. Geochem. Geophys. Geosystem 2. doi:10.1029/2001GC000183.

Nagle, F., 1966. Geology of the Puerto Plata area, Dominican Republic. PhD Thesis: Princeton, New Jersey, Princeton University, 171 pp.

Okamoto, A., Toriumi, M., 2001. Application of differential thermodynamics (Gibbs' method) to amphibole zonings in the metabasic system. Contrib. Mineral. Petrol. 141, 268–286.

Parra, T., Vidal, O., Agard, P., 2002. A thermodynamic model for Fe–Mg dioctahedral K-white micas using data from phase equilibrium experiments and natural pelitic assemblages. Contrib. Mineral. Petrol. 143, 706–732.

Parrish, R.R., Carr, S.D., Parkinson, D.L., 1988. Eocene extensional tectonics and geochronology of the southern Omineca belt, British Colombia and Washington. Tectonics 7, 181–212.

Perchuk, A.L., Philippot, P., 2000. Nascent subduction: record in Yukon eclogites. Petrology 8, 1–16.

Perchuk, A., Gerya, T., 2005. Subsidence and exhumation dynamics of eclogites in the Yukon–Tanana Terrane, Canadian Cordillera: petrological reconstructions and geodynamic modeling. Petrology 13, 253–266.

Perchuk, A., Philippot, P., Erdmer, P., Fialin, M., 1999. Rates of thermal equilibration at the onset of subduction deduced from diffusion modeling of eclogitic garnets, Yukon-Tanana terrane, Canada. Geology 27, 531–534.

Philippot, P., Blichert-Toft, J., Perchuk, A.L., Costa, S., Gerasimov, V. Yu., 2001. Lu–Hf and Ar–Ar geochronology supports extreme rate of subduction zone metamorphism deduced from geospeedometry. Tectonophysics 342, 23–38.

Pindell, J.L., 1990. Geological arguments suggesting a Pacific origin for the Caribbean plate. In: Larue, D.K., Draper, G. (Eds.), Transactions of the 12th Caribbean Conference: St. Croix, 7-11 August, 1989, pp. 1–4.

Pindell, J.L., Dewey, J.F., 1982. Permo–Triassic reconstruction of western Pangea and the evolution of the Gulf of Mexico–Caribbean region. Tectonics 1, 179–211.

Pindell, J.L., Draper, G., 1991. Stratigraphy and geological history of the Puerto Plata area, northern Dominican Republic. Spec. Pap. - Geol. Soc. Am. 262, 97–114.

Pindell, J.L., Kennan, L., 2001. Kinematic evolution of the Gulf of Mexico and Caribbean, in Petroleum systems of deep water basins: global and Gulf of Mexico experience. Proceedings Gulf Coast Section, SEPM 21st Anniversary Research Conference, Dec 2-5. Society for Sedimentary Geology (SEPM), Houston Texas, pp. 193–220.

Pindell, J.L., Kennan, L., Maresch, W.V., Stanek, K–P., Draper, G., Higgs, R., 2005. Plate kinematics and crustal dynamics of circum-Caribbean arc-continent interactions: tectonic controls on basin development in Proto-Caribbean margins. Spec. Pap. - Geol. Soc. Am. 394, 7–52.

Powell, R., Holland, T.B.J., 1994. Optimal geothermometry and geobarometry. Am. Mineral. 79, 120–133.

Powell, R., Holland, T.B.J., 1999. Relating formulations of the thermodynamics of mineral solid solutions: activity modeling of pyroxenes, amphiboles and micas. Am. Mineral. 84, 1–14.

Scherer, E.E., Cameron, K.L., Blichert-Toft, J., 2000. Lu–Hf garnet geochronology: closure temperature relative to the Sm–Nd system and the effects of trace mineral inclusions. Geochim. Cosmochim. Acta 64, 3413–3432.

Scherer, E., Münker, C., Mezger, K., 2001. Calibration of the lutetium-hafnium clock. Science 293, 683–687.

Schmidt, M.W., Poli, S., 1998. Experimentally based water budgets for dehydrating slabs and consequences for arc magma generation. Earth Planet. Sci. Lett. 163, 361–379.

Schwartz, S., Allemand, P., Guillot, S., 2001. Numerical model of the effect of serpentinization on the exhumation of eclogitic rocks: insights from the Monviso ophilitic massif (Western Alps). Tectonophysics 342, 193–206.

Shreve, R.L., Cloos, M., 1986. Dynamics of sediment subduction, melange formation, and prism accretion. J. Geophys. Res. 91, 10229–10245.

Sisson, V.B., Harlow, G.E., Avé Lallemant, H.G., Hemming, S., Sorenson, S.S., 2003. Two belts of jadeitite and other high-pressure rocks in serpentinites, Motagua fault zone Guatemala. Abstr. - Geol. Soc. Am. 35 (4), 75.

Smith, C.A., Sisson, V.B., Avé Lallemant, H.G.A., Copeland, P., 1999. Two contrasting pressure–temperature–time paths in the Villa de Cura blueschist belt, Venezuela: possible evidence for Late Cretaceous initiation of subduction in the Caribbean. Geol. Soc. Amer. Bull. 111, 831–848.

Stacey, J.S., Kramers, J.D., 1975. Approximation of terrestrial lead isotope evolution by a two stage model. Earth Planet. Sci. Lett. 26, 207–221.

Stöckhert, B., 2002. Stress and deformation in subduction zones-insight from the record of exhumed high pressure metamorphic rocks. In: de Meer, S., et al. (Ed.), Deformation Mechanisms, Rheology, and Tectonics: Current Status and Future Perspectives. Spec. Publ. - Geol. Soc., 200, pp. 255–274.

Stöckhert, B., Gerya, T., 2005. Pre-collisional high pressure metamorphism and nappe tectonics at active continental margins: a numerical simulation. Terra Nova 17, 102–110.

Steiger, R.H., Jäger, E., 1977. Subcommission on geochronology: convention on the use of decay constants in geo- and cosmochronology. Earth Planet. Sci. Lett. 36, 359–362.

Thöni, M., Jagoutz, E., 1992. Some new aspects of dating eclogites in orogenic belts: Sm–Nd, Rb–Sr, and Pb–Pb isotopic results from the Austroalpine Saualpe and Koralpe type-locality (Carinthia/Styria, southeastern Austria). Geochim. Cosmochim. Acta 56, 347–368.

Vance, D., Holland, T.J.B., 1993. A detailed isotopic and petrological study of a single garnet from the Gassetts Schist, Vermont. Cotrib. Mineral. Petrol. 114, 101–118.

Vidal, O., Parra, T., Trotet, F., 2001. A thermodynamic model for Fe–Mg aluminous chlorite using data from Phase equilibrium experiments and natural pelitic assemblages in the 100–600 °C, 1–25 kbar range. Am. J. Sci. 6, 557–592.

Villa, I.M., 1998. Isotopic closure. Terra Nova 10, 42–47.

Vinograd, V.L., 2002a. Thermodynamics of mixing and ordering in the diopside-jadeite system. I. ACVM model. Mineral. Mag. 66, 513–536.

Vinograd, V.L., 2002b. Thermodynamics of mixing and ordering in the diopside-jadeite system. II. A polynomial fit to the CVM results. Mineral. Mag. 66, 537–545.

Wakabayashi, J., 1990. Counterclockwise P–T–t paths from amphibolites, Franciscan Complex, California: relics from the early stages of subduction zone metamorphism. J.Geol. 98, 657–680.

Waters, D.J., Martin, H.N., 1993. Geobarometry in phengite-bearing eclogites. Terra Abstr. 5, 410–411.

Wei, C.J., Powell, R., Zhang, L.F., 2003. Eclogites from the south Tianshan, NW China: petrological characteristic and calculated mineral equilibria in the $Na_2O–CaO–FeO–MgO–Al_2O_3–SiO_2–H_2O$ system. J. Metamorph. Geol. 21, 163–179.

Will, T.M., Powell, R., 1992. Activity-composition relationships in multicomponent amphiboles: an application of Darken's quadratic formalism. Am. Mineral. 77, 954–966.

Will, T., Okrusch, M., Schmädicke, E., Chen, G., 1998. Phase relations in the greenschist-blueschist-amphibolite-eclogite facies in the system $Na_2O–CaO–FeO–MgO–Al_2O_3–SiO_2–H_2O$ (NCFMASH), with application to metamorphic rocks from Samos, Greece. Contrib. Mineral. Petrol. 132, 85–102.

Wunder, B., Schreyer, W., 1997. Antigorite: High-pressure stability in the system $MgO–SiO_2–H_2O$ (MSH). Lithos 41, 213–227.

York, D., 1969. Least squares fitting of a straight line with correlated errors. Earth Planet. Sci. Lett. 5, 320–324.



Please cite this article as: Krebs, M., et al., The dynamics of intra-oceanic subduction zones: A direct comparison between fossil petrological evidence (Rio San Juan Complex, Dominican Republic) and numerical simulation, Lithos (2007), doi:10.1016/j.lithos.2007.09.003